The Astrophysical Journal Supplement Series, 187:228–250, 2010 March doi:10.1088/0067-0049/187/1/228

A SYSTEMATIC STUDY OF Hα PROFILES OF Be STARS

J. Silaj[1], C. E. Jones[1], C. Tycner[2], T. A. A. Sigut[1], and A. D. Smith[2]
[1] Department of Physics and Astronomy, The University of Western Ontario, London, Ontario, N6A 3K7, Canada
[2] Department of Physics, Central Michigan University, Mt. Pleasant, MI 48859, USA
Received 2009 August 24; accepted 2010 February 4; published 2010 March 3

ABSTRACT

We present a set of theoretical Hα emission-line profiles of Be stars, created by systematically varying model input parameters over a wide range of accepted values. Models were generated with a non-LTE radiative transfer code that incorporates a non-isothermal disk structure and a solar-type chemical composition. The theoretical Hα emission-line profiles were compared to a large set of Be star spectra with the aim of reproducing their global characteristics. We find that the observed profile shapes cannot be used to uniquely determine the inclination angle of Be star+disk systems. Drastically different profile shapes arise at a given inclination angle as a direct result of the state of the gas, and self-consistent disk physical conditions are therefore crucial for interpreting the observations.

Key words: circumstellar matter – line: formation – line: profiles – stars: emission-line, Be

Online-only material: color figures, machine-readable table

1. INTRODUCTION

Classical Be stars are non-supergiant B-type stars whose spectra have, or have had at some time, one or more emission lines in the Balmer series. In particular, the Hα emission line is typically the dominant feature in the spectra of such stars, and many authors have modeled Hα line profiles to better understand the Be star phenomenon.

The emission lines in the spectra of Be stars arise from recombination in a flattened circumstellar disk (Quirrenbach et al. 1997; Tycner et al. 2005), a model first proposed by Struve (1931) and widely accepted since that time. The disk is composed of gaseous material and contains little or no dust, unlike the dusty disks surrounding young stars and protostars. While it is largely accepted that the disk is a decretion disk, i.e., the source of the disk material is the central star, the details of how the disk is created and maintained are not clear. A very rapidly rotating central star could explain the disk (or at least be one of the key factors in creating the disk), and in fact Be stars are known to have higher rotational velocities than a sample of normal B-type stars. Porter (1996) found the distribution of rotational velocities of a sample of Be stars to be sharply peaked at $\sim 0.7 v_{\rm crit}$, and Townsend et al. (2004) found that the rotational velocities of Be stars may be systematically underestimated, and that many may be rotating much closer than this to their critical velocity. Cranmer (2005) found a lower limit of 0.4–0.6$v_{\rm crit}$ for the rotational velocities of early-type (07e-B2e) Be stars, with the lower limit progressively rising for later-type (B3e-A0e) Be stars, ultimately reaching $v_{\rm crit}$ for the coolest Be stars.

The observed emission lines take a variety of shapes, from wine bottle profiles, singly or doubly peaked profiles, to shell spectra (Hanuschik et al. 1996). (Throughout this paper we adopt the convention, as proposed by Hanuschik et al. (1996), that to qualify as a shell star the central absorption must extend below the stellar continuum flux.) The traditional explanation for the variation in observed line profile shapes is a dependency on i, the inclination angle of the star's pole to the observer's line of sight (i.e., $i = 0^\circ$ is pole-on and $i = 90^\circ$ is equator-on). In the rotation model of Struve (1931), schematically illustrated in Figure 3 of Slettebak (1979), shell profiles occur only for cases where the disk is viewed edge-on, and singly peaked and wine bottle profiles occur only for near pole-on viewings, while doubly peaked profiles occur at mid-inclination angles. This paradigm is very much accepted and line profile shapes are commonly used in the literature to infer inclination angles, although a few authors (see, e.g., Quirrenbach et al. 1997; Miroshnichenko et al. 2001) have cautioned that line profile shapes cannot always be used to accurately determine inclination angles.

A further feature of Be emission profiles is that all of the aforementioned shapes have been observed in both symmetric and asymmetric forms. The current leading theory is that asymmetric profiles arise from one-armed density waves in the circumstellar disk, which is also known as the global disk oscillation model. Recently, Carciofi et al. (2009) successfully reproduced most of the observational features of ζ Tau, a Be star with a semi-stable cycle in asymmetric line profile variation, using the disk oscillation model of Okazaki (1997) and Papaloizou et al. (1992). In this model, a one-armed $m = 1$ oscillation mode is superposed on an unperturbed, axisymmetric disk. Thus we propose that asymmetric profiles can be considered a superset of the symmetric profiles, and that any of the fundamental results obtained for symmetric profiles (such as profile shape, relative line intensity, and equivalent width) could be extended to asymmetric profile shapes with the addition of another layer of complexity to the models.

Another notable aspect of Be star emission is its variability. While some stars exhibit emission that is virtually constant over periods as long as decades, many Be stars exhibit variations in their emission. For example, a significant portion (about 1/3) of all doubly peaked profiles exhibit changing asymmetry (Hanuschik et al. 1996), with the so-called violet-to-red ratio (V/R) being cyclically variable on timescales of years to decades. Furthermore, Be stars can change from stable V = R configurations to V/R variability and back. Some Be stars have been observed to lose their Hα emission completely, only to regain it at a later time (Porter & Rivinius 2003).

Perhaps more interestingly, some stars have shown transitions from one profile shape to another. Hanuschik (1986) noted that Hα profiles can transition between singly peaked and doubly peaked structures. There are also several Be stars (for example, γ Cas (Cowley & Marlborough 1968), Pleione (Gulliver 1977; Cramer et al. 1995; Hanuschik et al. 1996), and 59 Cyg (Barker

1982)) that have been observed to transition from shell spectra to emission-line spectra and vice versa. It has been suggested that these transitions are a result of dynamical effects due to the misalignment of the disk orbital plane and the stellar equator (see Porter & Rivinius 2003). However, we focus on the changes in line profile types as disk thermal structure evolves with variations in density, demonstrating that different types can appear due to density changes alone.

Detailed modeling of the Hα line, using a realistic physical model and the self-consistent, non-LTE code BEDISK, has now been performed for several well-known Be stars: γ Cassiopeiae (Sigut & Jones 2007), χ Ophiuchi (Tycner et al. 2008), κ Draconis, β Pisces, and υ Cygnus (Jones et al. 2008). These models successfully reproduce the observations, and provide valuable insight into the physical conditions of Be star+disk systems. Having completed these careful studies, we now propose to take a more global view of Be star emission profiles and instead of modeling the minutiae of individual spectra, we focus on reproducing the general features of a large set of observed Hα emission lines. Although there have been previous studies that have considered the parameter dependence on the Hα profile types (see, for example, Hummel & Vrancken 2000; Iwamatsu & Hirata 2008), in this work the disk thermal structure, critical to the state of the disk gas, is taken into account self-consistently.

To accomplish this task, we created a set of theoretical disk models by systematically varying the input parameters in small steps over a wide range of values. The spectral type of the central star was varied from B0 to B8, and for each disk model, the line profiles that would result if the disk was inclined to the observer at $i = 20°$, 45°, and 70° were computed. Next, the theoretical profiles were matched to a large set of observations. This accomplishes several important objectives: it allows us to determine the (approximate) physical conditions in a large number of Be stars, develops our intuitive understanding of emission-line profiles and how their appearance changes with changing physical conditions, and aids us in identifying which values are typical for the model parameters, and similarly which combinations of model parameters produce realistic/unrealistic models. This is the first time a study of this nature has been done with non-isothermal disks.

2. THEORY

The calculations in this paper were performed with a non-local thermodynamic equilibrium (non-LTE) code, BEDISK, developed by Sigut & Jones (2007). BEDISK computes hydrogen line spectra and the overall spectral energy distribution (SED) of the disk. An overview of the code is given below, and assumptions in the code relevant to this work are also discussed. For further details, the reader is referred to Sigut & Jones (2007).

The circumstellar disk is assumed to be axisymmetric about the star's rotation axis and symmetric about the midplane of the disk. We use R to denote the radial distance from the star's rotation axis and Z for the height above the equatorial plane. Following the works of Waters (1986), Coté & Waters (1987) and Waters et al. (1987), the radial density in the equatorial plane is assumed to decrease according to an R^{-n} power law. The vertical density distribution of the disk is found by assuming approximate hydrostatic equilibrium in the Z-direction: the gas pressure gradient balances the Z-component of the star's gravitational acceleration. Thus, the density distribution takes the form:

$$\rho(R, Z) = \rho_0 \left(\frac{R_*}{R}\right)^n e^{-(Z/H)^2}, \quad (1)$$

where ρ_0 is the disk base-density in the equatorial plane, n is the index of the radial power law, and H is the scale height in the Z-direction and is given by

$$H = \sqrt{\frac{2R^3}{\alpha_0}}, \quad (2)$$

where the parameter α_0 is of the form

$$\alpha_0 = GM_* \frac{\mu_0 m_H}{kT_0}. \quad (3)$$

In these expressions, M_* and R_* are the stellar mass and radius, respectively, and T_0 and μ_0 are the assumed initial temperature and mean molecular weight of the gas at the radial distance R.

Combining this density model with the photoionizing radiation field from the central star, the equations of statistical equilibrium are solved for each atom and ion included in the model. The code uses realistic solar abundances taken from Anders & Grevesse (1989) and Anders & Noels (1993); this is an important detail because while the disk is composed largely of hydrogen and helium, even small amounts of heavier elements can significantly impact heating and cooling rates. Rates of energy gain and loss are determined at each computational grid point, and temperatures are iterated to enforce radiative equilibrium.

In order to obtain this thermal solution, hydrogen level populations are computed. Thus, the Hα line emissivity and opacity,

$$\eta_\nu^{32} = \frac{h\nu_{23}}{4\pi} N_3 A_{32} \phi_\nu \quad (4)$$

and

$$\chi_\nu^{32} = \frac{h\nu_{23}}{4\pi} (N_2 B_{23} - N_3 B_{32}) \phi_\nu, \quad (5)$$

are known at each (R, Z) location in the disk. Here N_2 and N_3 are the hydrogen number densities in levels 2 and 3, respectively, A_{32}, B_{23}, and B_{32} are the Einstein probability coefficients for Hα, and ϕ_ν is the Hα line profile. Continuous free–free and bound-free emissivity and opacity of hydrogen was added to Equations (4) and (5) to obtain the total emissivity and opacity at the frequency of Hα. Electron scattering was also included as a coherent source of opacity, but not as a source of emissivity.

To calculate the Hα line profile in Equations (4) and (5), the Stark broadening routines of Barklem & Piskunov (2003) were used. These routines also include the contributions of (thermal) Doppler broadening and other collisional broadening, and can handle high disk densities for which the assumption of a simple Gaussian or Voigt profile would be invalid. We note that we have neglected the effect of sheer broadening on the Hα line profiles. This effect was studied by Hummel & Vrancken (2000) for Be star emission lines following the theory developed by Horne & Marsh (1986) for accretion disks. Nevertheless, Hummel & Vrancken (2000) conclude that even for an inclination of 80°, the effect on a hydrogen line profile is not large. The maximum inclination angle we use in this study is 70° and only 3 stars out of the 56 models are fit by this larger inclination. Therefore, the neglect of this effect is not significant in this work.

To compute the resultant theoretical Hα profile for the star+disk system, we solved the transfer equation at each radial distance R along a ray in the Z-direction as viewed at an angle

Table 1
Adopted Stellar Parameters

Spectral Type	Stellar Radius ($R_\odot$)	Stellar Mass ($M_\odot$)	$T_{\rm eff}$ (K)	log g
B0	10.00	17.00	25,000	4.0
B2	5.33	9.11	21,000	4.0
B5	3.90	5.90	15,000	4.0
B8	3.00	3.80	12,000	4.0

i relative to the line of sight. For rays terminating on the stellar surface, we adopted a photospheric Hα line profile computed using the code of Barklem & Piskunov (2003). For rays passing through the disk, the equation of radiative transfer,

$$\frac{dI_\nu(R, Z)}{dZ} = \eta_\nu^{32} - \chi_\nu^{23} I_\nu(R, Z), \quad (6)$$

was solved with the short characteristic method of Olson & Kunasz (1987). The disk was assumed to be in pure Keplerian rotation. We emphasize that the Hα profiles in our work are found from the same solution of the radiative equilibrium temperature structure for the disk, and that our approach therefore retains the full dependence of the physical conditions in the disk on the resultant Hα profile and is self-consistent.

3. MODELS

Be stars represent about 15% of all B stars, although they are more common among the earlier type B stars than later type B stars, with peak incidence occurring at the B1e-B2e spectral type (Porter & Rivinius 2003). While it is not clear why Be stars occur preferentially at earlier spectral types, in order to properly represent them in our theoretical models we included both the B0 and B2 subclasses. The B5 and B8 subclasses were chosen to approximately represent mid- and late-type B stars, respectively.

γ Cassiopeiae (HD 5394; B0 IVe) was the first reported Be star, detected by Padre Angelo Secchi in 1866 (Secchi 1867), and for many years was considered a prototypical classical Be star. It has since been shown to be a rather unusual star, exhibiting light, color, line-profile, and radial velocity variations, as well as unique X-ray and IR characteristics (see Harmanec (2002) for a full discussion of γ Cas). Nonetheless, it is a well-studied star, and it has also been previously modeled by some of the authors (see Sigut & Jones 2007). Thus, we take the mass, radius, and effective temperature of γ Cas to be representative of the B0 class of stars for ease of comparison with previous work. For the B2, B5, and B8 models, we take interpolated values of mass, radius, and effective temperature from Cox (2000). See Table 1 for adopted values.

The final component of the model which must be set in advance is the equatorial velocity, $v_{\rm eq}$. Because the ultimate goal of this study is to compare our theoretical models with observations, we elected to hold $v \sin i$ (the observable) constant and let $v_{\rm eq}$ vary with i. As Be stars are fast rotators, we initially adopted 300 kms^{-1} as a representative value for $v \sin i$; this results in reasonable $v_{\rm eq}$ values for $i = 45^\circ$ and $i = 70^\circ$, but makes $v_{\rm eq}$ significantly larger than $v_{\rm crit}$ when $i = 20^\circ$. To remedy the situation, $v \sin i = 150$ kms^{-1} was adopted for the $i = 20^\circ$ case. The chosen $v \sin i$ values were kept constant with changing spectral type; this was done to minimize the number of variables in the models. This has the additional effect of causing $v_{\rm eq}$ to vary from $\sim$0.6–0.8$v_{\rm crit}$ for the earliest spectral type to $v_{\rm eq} \approx v_{\rm crit}$ for the latest spectral type, which is in agreement with the findings of Cranmer (2005).

All of our models were computed using a (36, 30) (R, Z) grid with a solar composition. The computational grid is tailored to each individual model; R grid points are computed in terms of R_* (starting at $R = 1.0R_*$, the stellar surface, and extending out to $R = 30.0R_*$), and the Z grid points extend from $Z = 0$ (the equatorial plane) to the Z-value at which $\rho(Z)/\rho(Z = 0) = 10^{-3}$. In both cases, the grid spacing is non-uniform so that near the stellar surface and near the equatorial plane, where changes are occurring most rapidly, the grid is quite fine. Grid points become progressively more widely spaced as both R and Z increase and conditions in the disk change more slowly. An investigation into the effect of a larger grid (i.e., finer spacing between grid points) found that the results obtained were nearly identical to those obtained with the (36, 30) (R, Z) grid, and since the larger grid requires significantly more computational time, it was not adopted. While adopting a solar composition (as opposed to assuming a pure hydrogen composition) does incur larger computational time, it represents a much more realistic model. The inclusion of metals results in additional heating and especially cooling processes which are not available to a pure hydrogen plasma (see, e.g., Jones et al. 2004; Sigut & Jones 2007), and can significantly change the disk's thermal structure, which in turn can affect the resultant model line profile.

Detailed modeling of Hα profiles by us and other authors using a simple power-law density distribution model (see Equation (1)) have typically found values for ρ_0 ranging from 1×10^{-12} g cm^{-3} to 1×10^{-10} g cm^{-3}, and n ranging from $\sim$2 to 4 (see, e.g., Jones et al. 2008). To be thorough, we have computed models with ρ_0 values of $5 \times 10^{-13}, 1 \times 10^{-12}, \ldots, 5 \times 10^{-10}$ g cm^{-3} for each n value of 1.5, 2.0, ..., 4.5, for each of the four spectral class divisions. Thus, we obtained 42 SEDs for each spectral class division. For each SED, we then computed the line profile as it would appear if the system was inclined to an observer at 20°, 45°, and 70° to represent low, mid, and high inclination angles, respectively. In total, we produced 504 synthetic Hα line profiles.

To properly compare our synthetic Hα line profiles with spectroscopic observations, they were convolved with a Gaussian of FWHM of 0.656 Å. This brings the resolving power of the computed profiles down to 10,000 to match the approximate resolving power of our observations, all of which were obtained with the echelle spectrograph at the Lowell Observatory's John S. Hall telescope. (See the Appendix for additional information regarding the observations.)

4. RESULTS

Our results include over a hundred theoretical Hα profiles for each spectral class division, and so for brevity we do not present all of the models here. Figures 1–3, however, show a large selection of the models created for B0 stars, and illustrate the effects of varying n, ρ_0, and i, which is discussed in detail in Section 4.1. In Section 4.2, we discuss the effect of varying the spectral type of the central star, and Section 4.3 presents the main findings of this work. Finally, modeling of the observations is discussed in Section 4.4.

4.1. Effect of n, ρ_0, and i

Examining the set of four plots for models based on B0 central stars and at $i = 20^\circ$ (Figure 1), we can see that there is a large range in the widths, intensities, and shapes of the models depending on the choice of power law n and disk base-density ρ_0. Singly, doubly and triply peaked profiles have all been

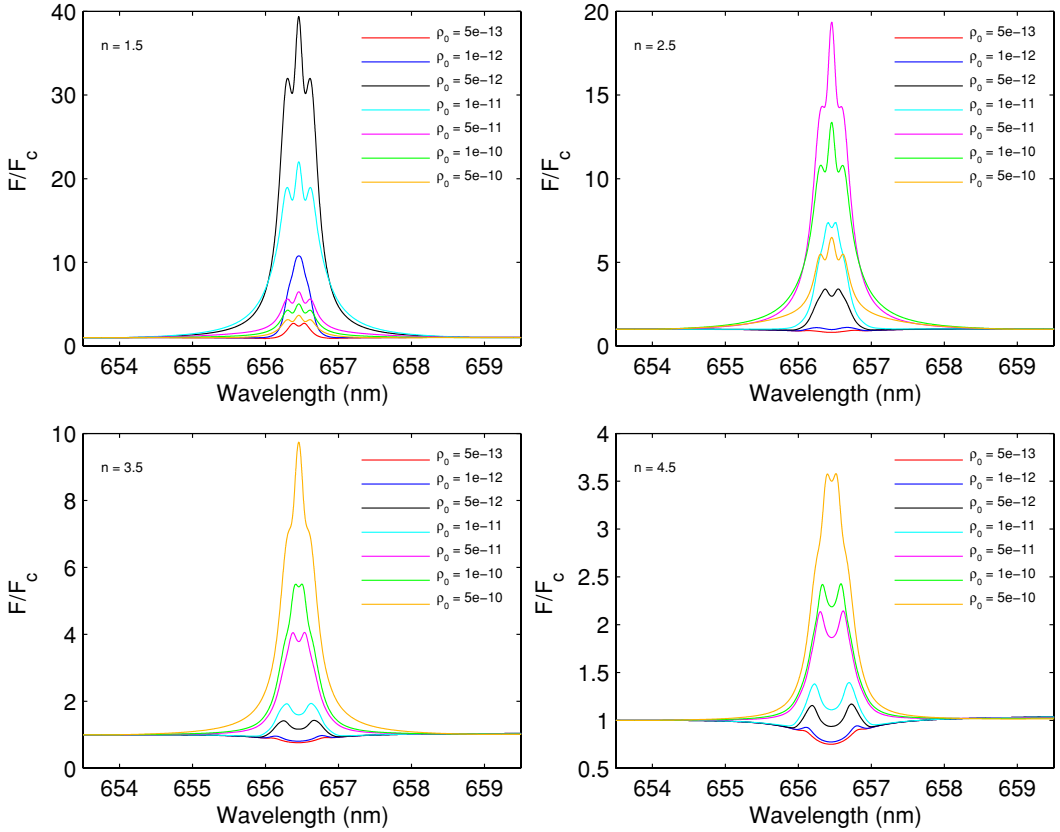

Figure 1. Representative sample of theoretical models created with a B0 central star and an inclination angle $i = 20^\circ$ for the star+disk system. n-values are indicated in the top left of each plot.

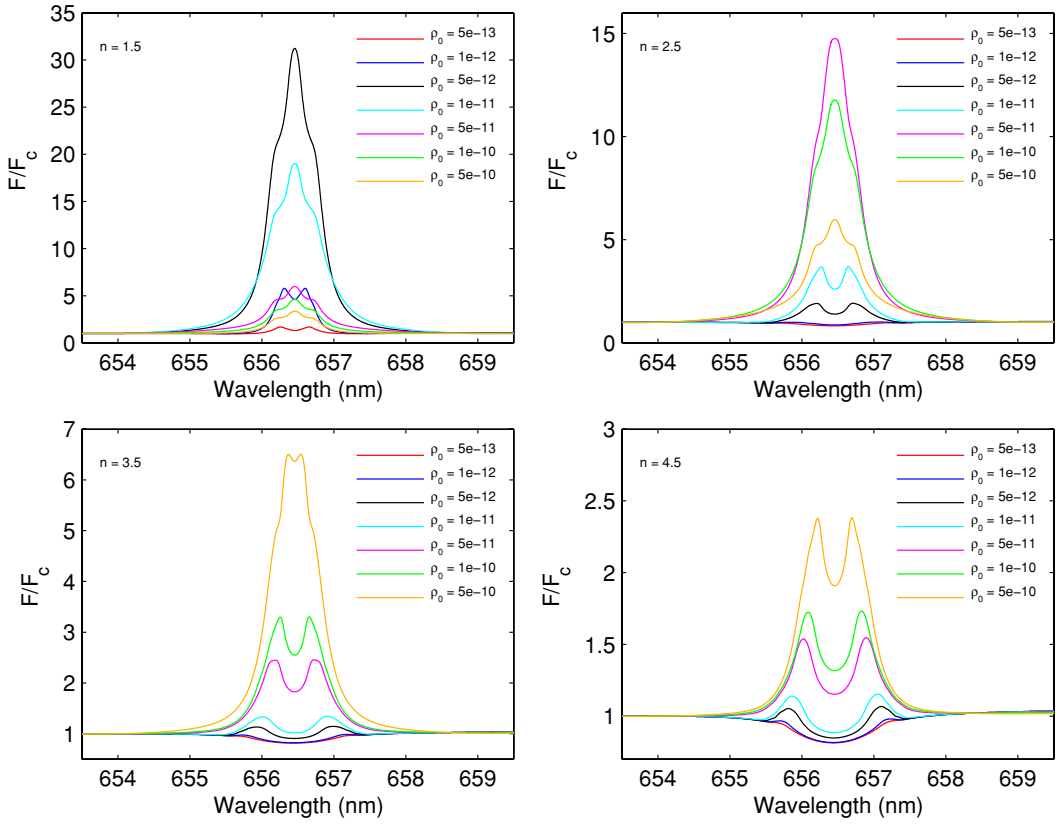

Figure 2. Representative sample of theoretical models created with a B0 central star and an inclination angle $i = 45^\circ$ for the star+disk system. n-values are indicated in the top left of each plot.

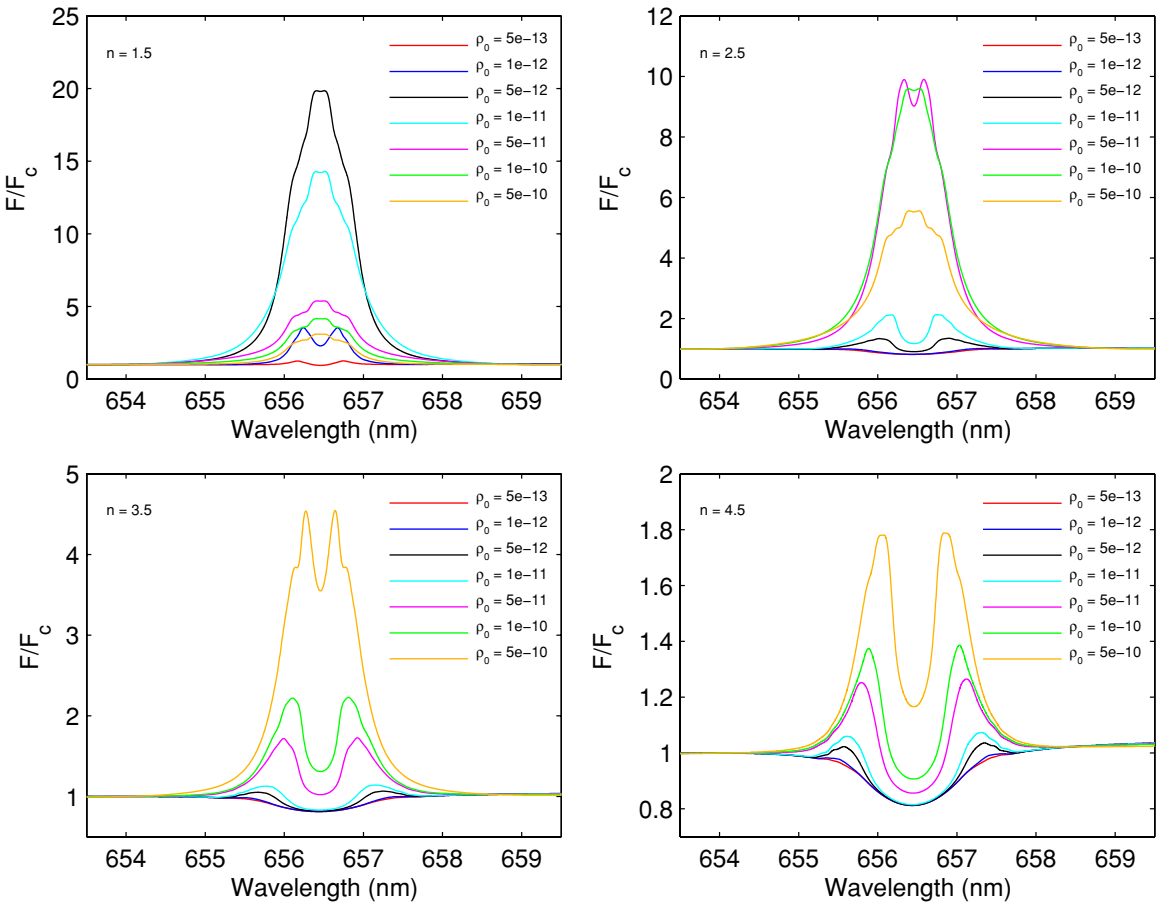

Figure 3. Representative sample of theoretical models created with a B0 central star and an inclination angle $i = 70^\circ$ for the star+disk system. n-values are indicated in the top left of each plot.

obtained at this low inclination angle, although it is interesting to note that in the $n = 4.5$ set of models, only doubly peaked profiles occur. With such a large value for n (meaning the disk base-density drops off rapidly with radial distance), there is not enough material to fill in the peak of the profile.

The range in relative intensity of the models is very large, but we can see the clear trend that increasing n has the effect of decreasing the maximum possible line strength that can be obtained. This result makes intuitive sense, because a faster decrease in density means there is less material close to the star to be ionized and contribute to the line.

Another interesting feature in Figure 1 is regarding the relationship of the disk base-density, ρ_0, to the intensity of the line. For $n = 1.5$, the largest intensity by far occurs for the model with a disk base-density of 5×10^{-12} g cm^{-3}, but for $n = 2.5$, it occurs for the model with a disk base-density of 5×10^{-11} g cm^{-3}. The models created with the highest disk base-density, 5×10^{-10} g cm^{-3}, actually produce only moderately strong lines in these two cases, which may seem a bit counterintuitive. What would perhaps naturally be expected is that the largest disk base-density produces the strongest lines, as we see in the $n = 3.5$ and $n = 4.5$ models, but a large disk base-density coupled with a slow fall-off (low n) actually impedes line formation. This is due to the large build-up of material that is so dense as to remain cool and neutral when large ρ_0 and small n are combined.

In Figure 2, the models are the same as the first set (Figure 1) except that they were computed with an inclination angle of $i = 45^\circ$. Similarly, in Figure 3, the models are created with all of the same inputs as those in Figures 1 and 2, but the inclination angle i has now been increased to 70°. It is useful to examine these three figures in sequence, as doing so illustrates how increasing i affects the resulting emission-line profile shape. First and most noticeably, increasing i results in broadened profiles with reduced relative intensities due to the effect of the faster projected rotation. When $i = 45^\circ$, we still obtain singly, doubly, and triply peaked profiles, so clearly the number of peaks in an emission-line profile is not solely a function of inclination angle. While we do not see triply peaked profiles when $i = 70^\circ$, we still see singly and doubly peaked profiles, which supports the previous statement. Furthermore, we speculate that the reason we do not see triply peaked profiles is due to the severe broadening effect, already noted, which has effectively smeared out finer structures. Examining these same three figures more closely, we see that regardless of the chosen i value, the red and blue models (corresponding to disk base-density values of 5×10^{-13} and 1×10^{-12} g cm^{-3}) only ever show emission when $n = 1.5$. Increasing n to 2.5 and beyond, the profiles actually become absorption profiles because the low ρ_0 values mean there is not enough material to create an emission line. This is an important result that gives a lower limit to the disk base-density values that can produce emission-line profiles in the power-law density model we have adopted here. Furthermore, this result could perhaps explain the phases of emission and absorption that some Be stars are observed to have: instead of the star completely losing and subsequently rebuilding its disk, it may well be that the disk simply becomes very diffuse between

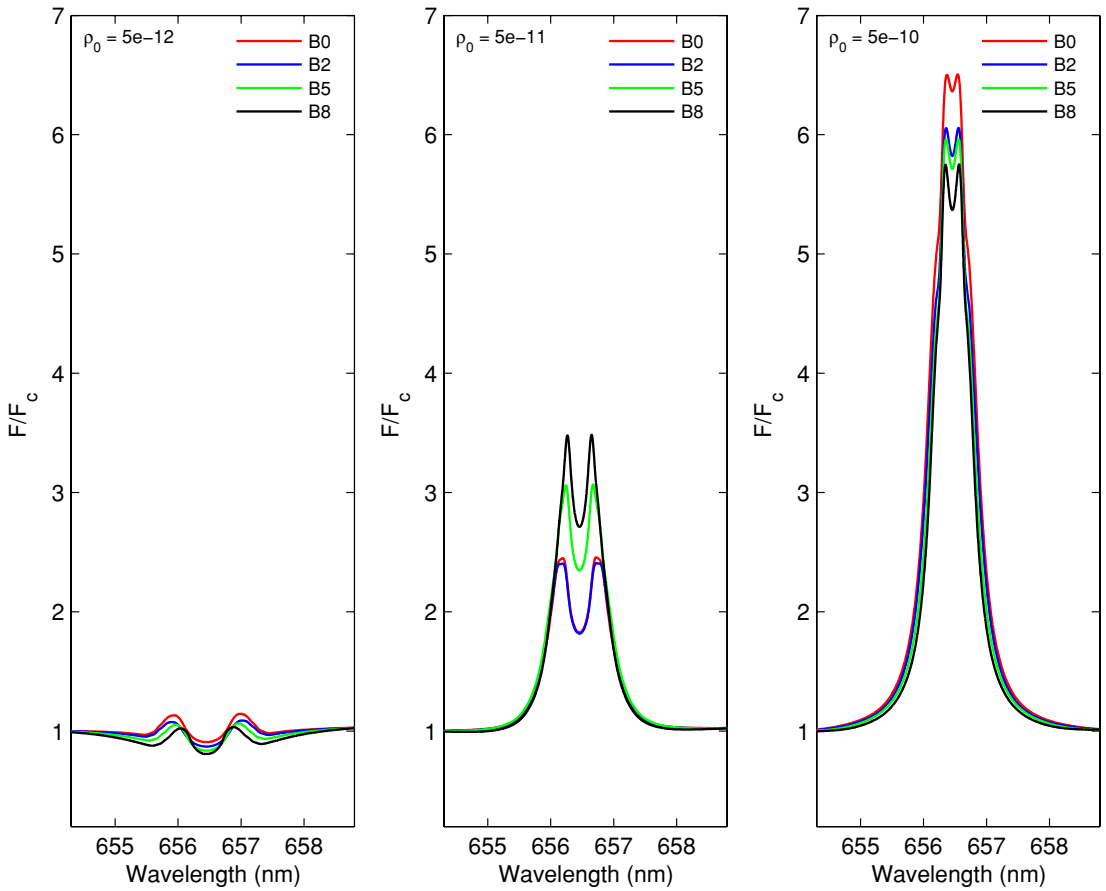

Figure 4. Effect of varying spectral type on the theoretical models. In each panel, $i = 45°$, $n = 3.5$, and disk base-density ρ_0 is as indicated in the top left of the panel.

periodic mass ejections from the central star and there is not enough emission from the disk to completely fill in the stellar absorption profile. This case is in agreement with the known variability of these systems.

4.2. Effect of Spectral Type

In Figure 4, we highlight the key effects of varying the spectral type. We adopt intermediate i and n values, and examine how the line profiles' appearance changes with spectral type for a low density ($\rho_0 = 5 \times 10^{-12}$), medium density ($\rho_0 = 5 \times 10^{-11}$), and high density ($\rho_0 = 5 \times 10^{-10}$) model.

Although it was found that the overall shape (i.e., number of peaks) of the theoretical profile was almost never affected by varying the spectral type, in each of the three panels of Figure 4 it can be seen that the overall width of the theoretical profile does decrease slightly for later spectral types. Normally, the biggest factor in profile width is the rotation rate, but since we held our rotation rate constant we are probably seeing a secondary (and much more subtle) effect: the physical disks associated with central stars of later spectral types are smaller than those associated with central stars of earlier spectral types.

In the first panel of Figure 4, the model profiles show little variation in shape and relative intensity with changing spectral type. This result is generally true for all of our models with the lowest disk base-densities.

Models with intermediate or high disk base-densities, however, show a stronger dependence on spectral type, and can become either more or less intense with decreasing spectral type. Specifically in Figure 4, the intermediate density models become more intense with decreasing spectral type while the high density models become less intense with decreasing spectral type. Examining the temperature structures for a large number of models with the same ρ_0 and n values, but varying spectral type, we found that the disks of the later type stars were sometimes hotter than those for the early-type stars (leading to higher intensities in the resultant models). When this occurs, the models behave as illustrated in the middle panel of Figure 4. However, nearly equally as often, the disks of the later type stars can also be cooler (leading to lower intensities in the resultant models, as shown in the rightmost panel of Figure 4). A model created with a central star of later spectral type has a different photoionizing radiation field because the central star is both smaller and cooler. As already mentioned, it will also have a correspondingly smaller Hα-emitting region. The interplay of these two factors is very intricate, and outcomes are not easy to predict. Sometimes the effect of the smaller emitting region dominates, and even though the photoionizing radiation field is a bit weaker, the model disk for a later type Be star will be hotter. Other times, the effect of having a cooler central star dominates, the star cannot heat the disk as efficiently as a central star of an earlier spectral type, and this results in a model profile that is less intense. This result emphasizes the importance of creating realistic and self-consistent models for Be stars.

4.3. Key Results

Figure 5 further illustrates the effect of increasing inclination angle i on the resulting emission-line profile. This figure shows doubly peaked profiles that were obtained at each of the three chosen i values. The lines become broadened, and have

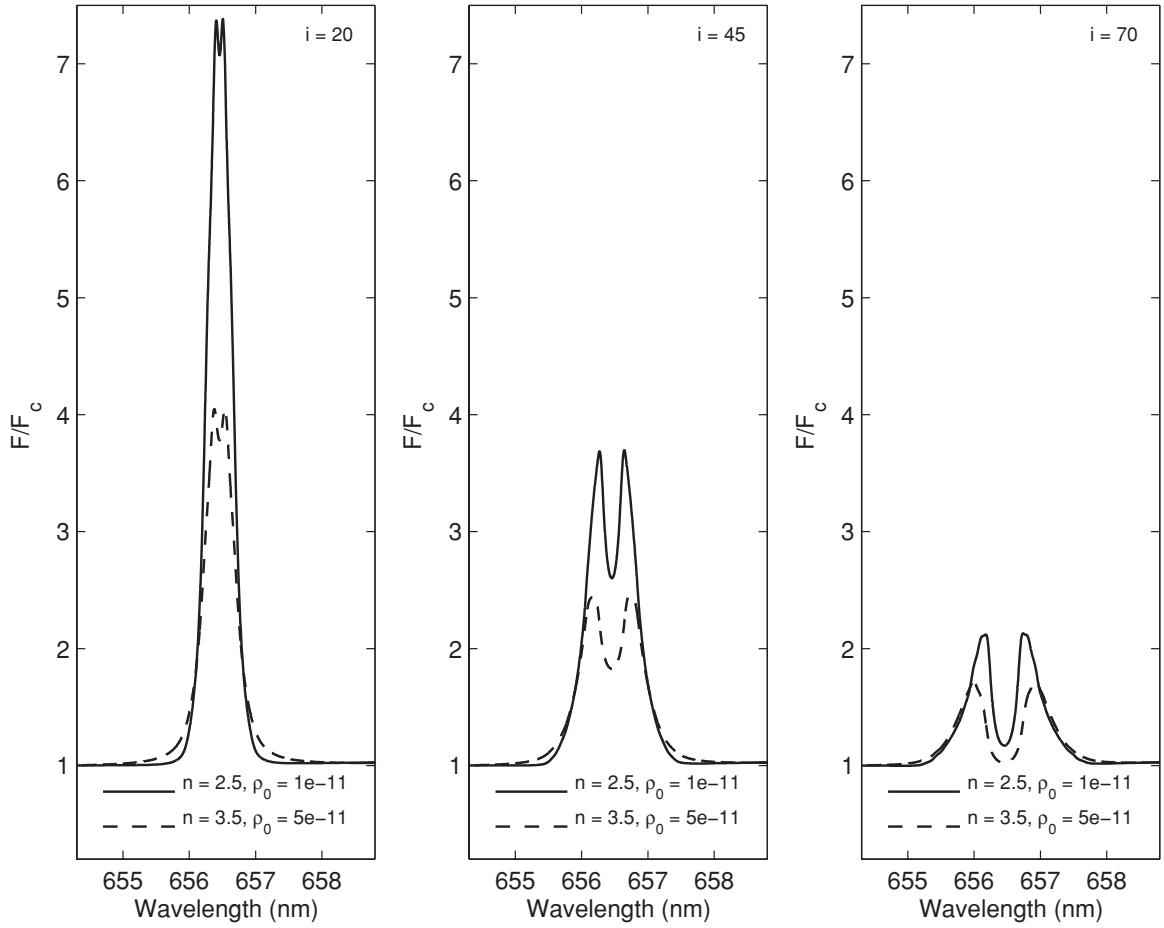

Figure 5. Doubly peaked models created at the three different inclination angles adopted for this study. The value of i is indicated in the top right of each panel.

Table 2
Model Disk Temperatures

Model[a]	i (°)	n	ρ_0 (g cm^{-3})	$T_{\rm min}$ (K)	$T_{\rm max}$ (K)	$T_{\rm avg}$ (K)[b]
1	20	1.5	1×10^{-12}	10453.6	16835.5	13339.7
2	20	4.0	5×10^{-11}	7843.0	17217.3	12132.9
3	45	2.5	5×10^{-11}	6025.1	17217.3	10146.0
4	45	2.5	1×10^{-11}	7602.3	16408.7	11863.9

Notes.
[a] Model numbers correspond, from top to bottom, to the models presented in Figure 6.
[b] This is a density-weighted average temperature for the disk.

lower relative intensities, with increasing i. This is a direct consequence of the projection of the disk.

Perhaps the most important result that has come of this modeling is the fact that we can obtain many different profile shapes at a single inclination angle i. (We note that to obtain singly peaked lines at the resolving power of the observations presented, the disk density must be relatively high for $n > 2.5$.) This point deserves further elaboration as, recalling the discussion of Struve's rotation model, it would seem highly unlikely to obtain such a result. However, it is important to recall that previous treatments of circumstellar disks considered them to be approximately isothermal, and our models produce self-consistent disk physical conditions. Examining the temperature structure graph in the top panel of Figure 6, for example, we see a clearly non-isothermal disk with the temperature variation being about 6000 K (see Table 2 for the minimum, maximum, and average disk temperatures of each model presented in Figure 6). The other three models in Figure 6 show even greater temperature variations. Thus, it is clear that isothermal disk models are a rather poor approximation, especially for the cases of higher density.

Comparing the profile and temperature structure in the second panel of Figure 6 with the top panel, the full effect of the overall state of the gas, including the temperature structure, in creating the spectral line emerges. As noted on the plot, both panels were created with $i = 20°$; the fact that we have obtained a singly peaked and a doubly peaked profile at the same inclination angle demonstrates that different profile types can be obtained by changes in disk density alone.

While the first two profiles in Figure 6 were obtained for very different values of n and ρ_0, small changes in one of the parameter values can sometimes have an equally drastic effect. The lower two profiles in Figure 6 were created with the same i and n values, and have ρ_0 values that differ only by a factor of a few (i.e., 5×10^{-11} g cm^{-3} versus 1×10^{-11} g cm^{-3}, respectively). The temperature profile in the third panel of Figure 6 has a cooler central region, but the disk base-density ρ_0 is high enough to fill in the central region of the corresponding line profile due to the warmer volumes of gas lying above and below this region. Also, even though the central region is cooler, the overall temperature variation in the disk is not as great as the temperature variation shown in the fourth panel. In the fourth panel of Figure 6, the disk base-density is slightly lower, and the central region of the line profile is no longer filled in. Also, this

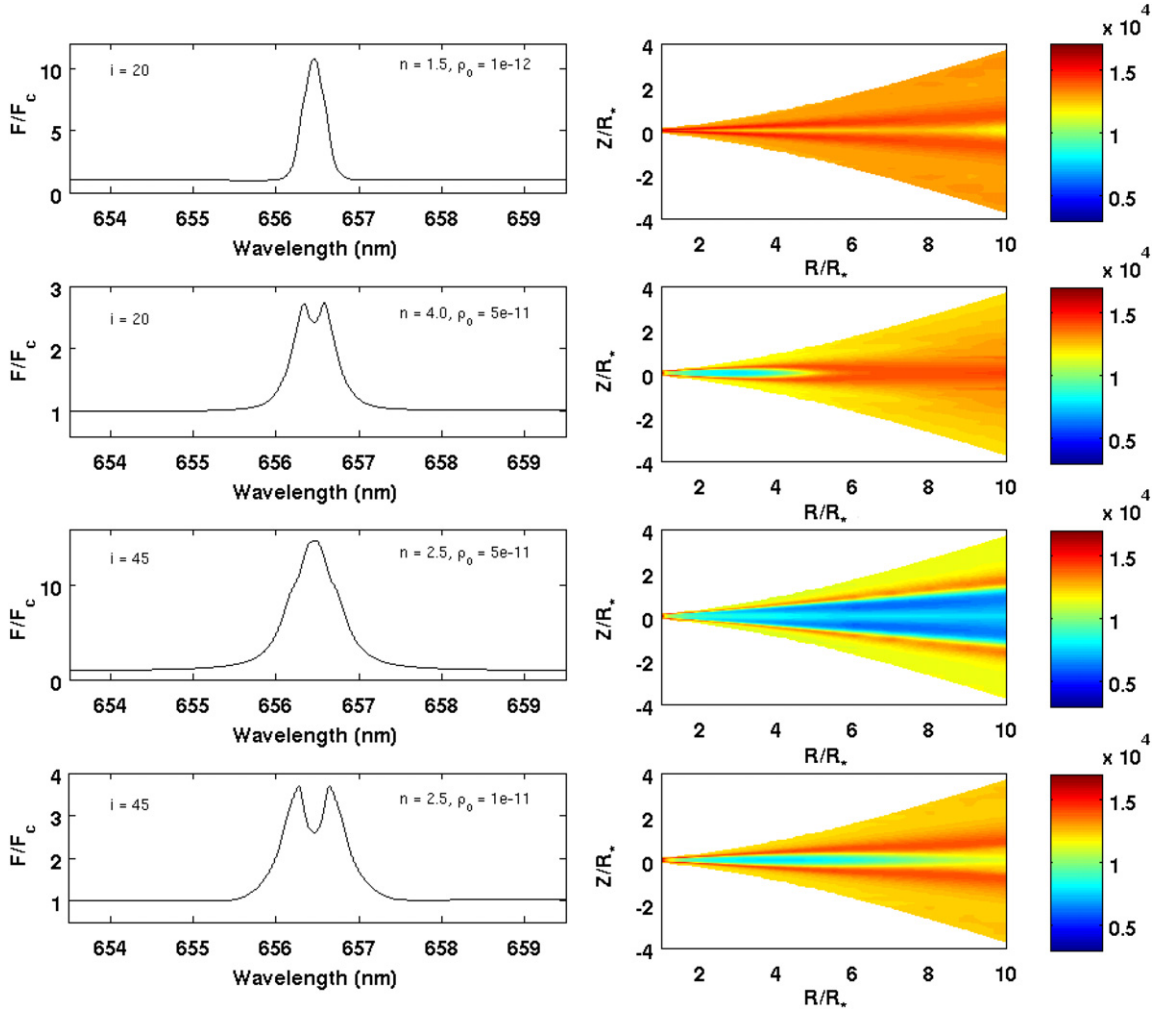

Figure 6. Line profiles (left) and their corresponding temperature structures (right) are shown for four different models. In each case, a B0 central star is assumed, and the model parameters i, n, and ρ_0 are as indicated on the profile plots. Note that while the models extend to $30R_*$, the temperature plots have been truncated to $10R_*$ to enlarge the area where greatest temperature variation is occurring. See Table 2 for the minimum, maximum, and (density-weighted) average temperature of each model shown here.

lower density allows some portions of the disk to be heated to very high temperatures, while the central region stays cool. The hot regions on either side of the central region are more efficient at emitting and create the doubly peaked line profile.

The fact that we can obtain different profile shapes at the same inclination angle offers an explanation for the observed transition between profile shapes that some Be stars have demonstrated. In this case, they would simply result from the changing physical conditions in the disk if the rate of material outflow from the star was variable, as it seems to be for some stars.

4.4. Modeling the Observations

We have preliminarily matched theoretical models from the set created for this paper to a catalog of Be star spectra. The chosen representative model for each spectrum is presented in Table 3. The representative models are also plotted with the observed spectra, which are presented in the appendix and available in Table 4. We again emphasize that the goal of the modeling is to reproduce the global features of the observed spectra and that we do not intend these models to be considered definitive.

Despite having only four representative spectral types, three inclination angles, and a fairly coarse grid of n and ρ_0 values from which to choose, we were able to find representative models that both matched the main features of the observed spectra and had good agreement between the equivalent widths for 46 of the 69 spectra. For an additional 10 spectra, satisfactory models were found once small alterations to the disk base-density ρ_0 were made; we opted to do this in the cases where an observed spectrum was clearly in between two of our existing models. Thus we have found representative models for ∼80% of the spectra based on the criteria of matching equivalent width simultaneously with profile shape. We did not model the remaining 13 spectra, either because they were shell spectra, or because they were highly asymmetric/unusual in some way. See the footnotes in Table 3 and Section 5 for further discussion of these spectra. We reiterate that we have chosen to model these stars with a coarse density grid to try to understand the significant features in the Hα profiles. Consequently, if one wished to match the Hα line for a particular star, a finer grid should be constructed to reduce the uncertainty, or range, in ρ_0 and n values. With our coarse grid, the uncertainty is a factor of 10 in ρ_0 and ± 0.5 in n. We note that, with these uncertainties, the work presented in this investigation is in reasonable agreement with the results for χ Ophiuchi (Tycner et al. 2008), κ Draconis, β Pisces, and υ Cygnus (Jones et al. 2008). It is also important to point out that the spectrum of χ Ophiuchi (a known variable)

Table 3
Representative Models

HR	HD	Star	Spectral Type[a]	EW (nm)[b]	Shape[c]	Model Parameters				
						Spectral Type[d]	$i(^\circ)$	n	ρ_0(g cm^{-3})	EW (nm)[e]
7	144	10 Cas	B9IVe	0.311	d	B8	20	3.5	5e-12	0.2602
193	4180	omi Cas	B5IIIe	−3.661	s	B5	20	3.5	1e-10	−3.1119
264	5394	gam Cas	B0IVe	−3.388	s	B0	45	1.5	1e-10	−2.94
335	6811	phi And	B7Ve	0.163	s	B8	20	2.0	8e-13	0.2174
496	10516	phi Per	B2Vpe	−3.185	d	B2	45	3.0	5e-11	−3.6732
985	20336	BK Cam	B2.5Vne	−1.598	d	B2	45	3.5	5e-11	−1.4809
1047	21455		B7V	−0.194	s	B8	20	2.0	1e-12	−0.0204[f]
1087	22192	psi Per	B5Ve	−4.236	d	B5	70	3.0	1e-10	−4.2816
1156	23480	23 Tau	B6IVe	0.158	d	B5	20	4.5	1e-11	0.1267
1160	23552		B8Vne	−0.216	d	B8	45	1.5	4e-13	0.0268[f]
1165	23630	eta Tau	B7IIIe	−0.298	d	B8	20	3.5	1e-11	−0.2918
1180	23862	28 Tau[g]	B8IVevar	−0.518	sh	...	...	...	...	...
1209	24534	X Per	O9.5pe	−2.865	s	B0	45	1.5	1e-10	−2.94
1273	25940	48 Per	B3Ve	−2.860	s	B2	20	2.5	1e-11	−2.6355
1423	28497	28 Eri	B1Ve	−1.240	d	B0	45	4.0	1e-10	−1.1582
1508	30076	56 Eri	B2Ve	−4.655	s	B2	20	3.5	5e-10	−4.2765
1605	31964	eps Aur[g]	A8Iab	0.090	sh	...	...	...	...	...
1622	32343	11 Cam	B2.5Ve	−2.171	s	B2	20	2.5	1e-11	−2.6355
1660	32991	105 Tau	B3Ve	−4.364	s	B2	20	3.5	5e-10	−4.4349
1789	35439	25 Ori	B1Ve	−1.324	d	B0	45	3.5	5e-11	−1.4767
1858	36576	120 Tau	B1.5IVe	−4.326	s	B2	45	3.5	5e-10	−4.3501
1910	37202	zet Tau[h]	B2IVe	−1.813	tr	...	...	...	...	...
1934	37490	ome Ori	B2IIIe	−0.501	d	B2	20	3.5	1e-11	−0.2802
2284	44458	FR CMa	B1.5IVe	−3.601	d	B2	45	3.0	5e-11	−3.6732
2343	45542	nu. Gem[g]	B6IIIe	−0.078	sh	...	...	...	...	...
2538	50013	kap CMa	B1.5IVe	−2.279	d	B2	20	3.5	5e-11	−1.868
2749	56139	ome CMa	B2IV-Ve	−2.323	s	B2	20	1.5	9e-13	−2.3092
2825	58343	FW CMa	B3Ve	−1.503	s	B2	20	1.5	7e-13	−1.1593
2845	58715	bet Cmi	B8Ve	−0.195	d	B8	20	3.5	9e-12	−0.1824
3034	63462	omi Pup	B1IV:nne	−1.533	s	B0	70	1.5	5e-10	−1.9476
3237	68980	r Pup	B1.5IVe	−3.405	s	B2	20	3.5	2e-10	−3.3846
3858	83953	I Hya	B5V	−2.016	d	B5	45	3.5	5e-11	−1.8928
3946	86612	OY Hya	B5Ve	−3.386	s	B5	20	3.5	1e-10	−3.1119
4123	91120		B9IVe	−0.045	d	B8	20	4.0	1e-11	0.0727
4696	107348	5 Crv	B8V	−0.366	d	B8	20	3.5	1e-11	−0.2918
4787	109387	kap Dra	B6IIIpe	−2.099	d	B5	45	4.0	5e-10	−2.338
5193	120324	mu Cen	B2Vnpe	−0.635	d	B2	20	2.5	5e-12	−0.8243
5440	127972	eta Cen	B1.5Vne	−1.058	d	B2	45	4.0	1e-10	−1.1387
5938	142926	4 Her[g]	B9pe	−0.113	sh	...	...	...	...	...
5953	143275	del Sco	B0.2IVe	−1.348	d	B0	20	4.0	1e-10	−1.3896
6118	148184	chi Oph	B2Vne	−5.525	s	B2	20	2.0	5e-12	−5.5033
6397	155806	V1075 Sco	O8Ve	−0.420	d	B0	20	3.5	1e-11	−0.4245
6519	158643	51 Oph[g]	A0V	0.323	sh	...	...	...	...	...
6664	162732	88 Her[g]	Bpshe	−0.688	sh	...	...	...	...	...
6712	164284	66 Oph	B2Ve	−0.365	d	B2	20	3.5	1e-11	−0.2802
7040	173370	4 Aql[g]	B9V	0.282	sh	...	...	...	...	...
7106	174638	bet Lyr[i]	B7Ve+...	−1.149	d	...	...	...	...	...
7708	191610	28 Cyg	B2.5Ve	−0.121	d	B2	45	1.5	5e-13	−0.1791
7836	195325	1 Del[g]	A1she...	0.463	sh	...	...	...	...	...
8047	200120	59 Cyg	B1.5Vnne	−1.328	s	B2	45	2.0	6e-10	−1.2241
8053	200310	60 Cyg[g]	B1Ve	0.008	sh	...	...	...	...	...
8146	202904	ups Cyg	B2Vne	−2.297	s	B2	20	3.5	1e-10	−2.484
8260	205637	eps Cap[g]	B3V:p	−0.248	sh	...	...	...	...	...
8402	209409	omi Aqr	B8IVe	−2.085	d	B8	45	3.5	5e-11	−1.9314
8438	210129	25 Peg	B6Ve	−0.386	d	B5	20	3.5	1e-11	−0.2947
8520	212076	31 Peg	B2IV-Ve	−2.855	s	B2	20	2.5	1e-11	−2.6355
8539	212571	pi Aqr	B1Ve	−0.298	d	B0	45	3.5	1e-11	−0.2064
8731	217050	EW Lac	B4IIIpe	−3.085	d	B5	70	3.5	5e-10	−3.2509
8773	217891	bet Psc	B6Ve	−0.933	s	B5	20	2.5	5e-12	−1.202
9070	224559	LQ And	B4Vne	−2.039	d	B5	45	4.0	5e-10	−2.338
	6343		B8	−0.554	s	B8	20	1.5	4e-13	−0.1767
	11606	V777 Cas	B2Vne	−2.185	tr	B2	20	3.5	5e-11	−1.868
	19243	V801 Cas	B1Ve	−3.845	s	B0	20	3.0	4e-11	−3.5458
	45314	PZ Gem	O9:pe	−2.326	d	B0	45	3.5	1e-10	−2.1955

Table 3
(Continued)

HR	HD	Star	Spectral Type[a]	EW (nm)[b]	Shape[c]	Model Parameters				
						Spectral Type[d]	$i(^\circ)$	n	ρ_0(g cm^{-3})	EW (nm)[e]
	53367	MWC 166[g]	B0IV:e	−0.075	sh	...	...	...	...	...
	141569		B9.5e	0.360	d	B8	20	4.0	9e-12	0.139
	163296	MWC 275	A1Ve	−1.529	s	B8	20	3.0	1e-11	−1.3085
	179218	MWC 614	B9e	−0.749	s	B8	20	1.5	5e-13	−0.6546
	206773		B0Vpe	−1.231	d	B0	45	4.0	5e-11	−0.8169

Notes.
[a] Taken from the SIMBAD Astronomical Database.
[b] Hα equivalent width based on observation, not corrected for tellurics. We adopt the standard convention that emission lines have negative area.
[c] Observed Hα line profile shape; s, single; d, double; tr, triple; sh, shell.
[d] Representative model spectral type. All models were created assuming a main-sequence (V) central star.
[e] Equivalent width value of the representative model.
[f] The discrepancy between the observed and calculated equivalent width is due to the continuum rectification, as there is significant cancellation between the positive and negative contributions.
[g] Due to the complexities of shell spectra, we have not applied a representative axisymmetric model to this star. For further discussion of shell spectra, see Section 5.
[h] Recent work on this star has demonstrated that there are variable overdense and underdense regions within the disk. Rotating spiral waves and global disk oscillations have been proposed (Wisniewski et al. 2007; Carciofi et al. 2009). Therefore, we have not applied a representative axisymmetric model to this star.
[i] Due to the highly asymmetric nature of this emission-line profile, a representative axisymmetric model has not been applied to it.

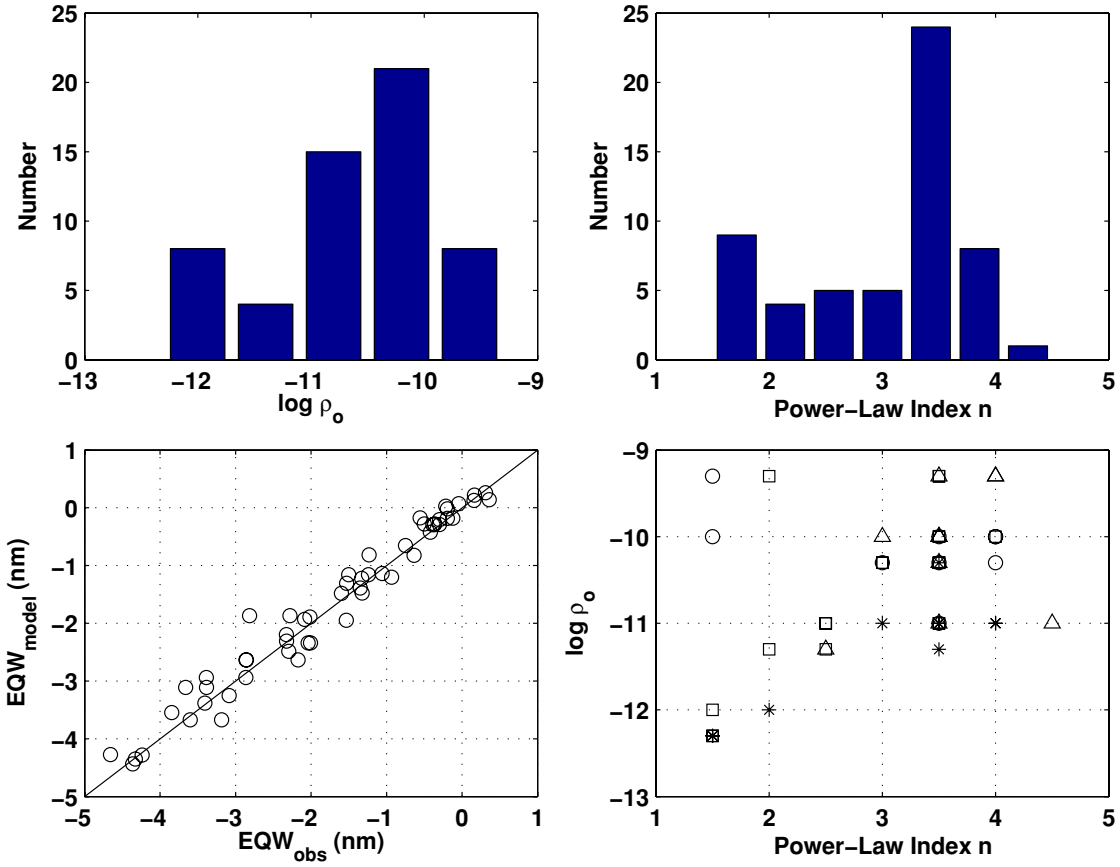

Figure 7. Summary of the model fits of Table 3. The top two panels show the distribution of disk base-densities (log ρ_o) and power-law indices (n) that parameterize the disk density (Equation (1)) for each model fit. The bottom left panel compares the observed and model Hα equivalent widths. The line in this figure is one of unit slope passing through the origin and is not a fit to the data. The bottom right panel shows, for each model fit of Table 3, the value of log ρ_o and n adopted. The symbols represent the different (fit) spectral types: B0 is a circle, B2 is a square, B5 is a triangle, and B8 is an asterisk.
(A color version of this figure is available in the online journal.)

that is presented in this paper was obtained approximately one year later than the spectrum presented in Tycner et al. (2008). During this time, the Hα equivalent width decreased from 7.1 nm to 5.5 nm.

The modeling has revealed that the plausible range of physical conditions (specifically, the disk base-density and its fall-off rate) in Be star disks is surprisingly large. Only a few combinations of n and ρ_0 (for example, $n = 1.5$ and

Table 4
Spectra

HR	HD	Star	Julian Date	λ (nm)	F/F_c
7	144	10 Cas	2453654.5	648.25159	0.93505926
				648.27600	0.91084650
				648.30029	0.90521774
				648.32458	0.91396274
				648.34900	0.90457700
				648.37329	0.92340855
				648.39758	0.93638472
				648.42194	0.94978650
				648.44617	0.94310843
				648.47052	0.95746975
				648.49475	0.95413687
				648.51910	0.94863946

(This table is available in its entirety in a machine-readable form in the online journal. A portion is shown here for guidance regarding its form and content.)

$\rho_0 = 5 \times 10^{-12}$; see Figure 1) produced unrealistic models that had no counterparts in the observations. All of the individual n and ρ_0 values from our initial grid, however, were employed in the modeling.

Figure 7 summarizes the model fits of Table 3. One interesting feature of the derived disk density parameters is that a radial power-law index of $n = 3.5$ is strongly preferred by the Hα fits. Over all stars considered, 43% of the fits require this power-law index. This result remains true over all of the (model) spectral types considered: 36% of the B0 fits, 45% of the B2 fits, 50% of the B5 fits, and 48% of the B8 fits, have $n = 3.5$. As seven values of the power-law index are represented in the model fits, this result is very unlikely to be due to chance alone. We note that an index of $n = 3.5$ is the minimum value required for an outflowing, isothermal viscous (decretion) disk (Porter 1999).

The bottom right panel explores any potential correlation between the derived values of $\log \rho_o$, the base-density of the disk, and the radial power-law index, n over the fits. Note that the lower-right portion of this plot is empty (low $\log \rho_o$ and large n) because such disks would be difficult to detect in Hα emission. With this bias in mind, there is no obvious correlation between the two parameters which fix the disk density distribution.

Finally, modeling the observations has clearly shown that profile shapes are not unique indicators of inclination angle. Examination of Table 3 reveals that doubly peaked profiles are often best matched by a representative model created at 20°, and many singly peaked profiles are best matched by a representative model created at 45°. What emerges from the modeling is that the width across the base of the profile is fairly sensitive to i (see Figure 5), and therefore some doubly peaked profiles simply cannot be matched by models created at higher inclination angles because the width across the base is absolutely too broad. Similarly, some broad, singly peaked profiles cannot be matched by models created with $i = 20°$ because all such models will be too narrow across the base of the profile.

5. CONCLUSIONS

We have presented a large set of systematically created theoretical Hα line profiles. By applying our models to a large set of observations, we have confirmed that they reproduce the global features found in actual spectra. Analysis of these representative profiles reveals that the interplay of the model parameters is often fairly complex, with outcomes that are difficult to predict. It is found that even small changes in the adopted initial values can greatly impact the temperature structure of the disk, which in turn affects resultant profile types. Based on these results, we find that profile types do not uniquely determine the inclination angle of a Be star+disk system. For example, we found that many singly peaked spectra were best represented by a model created at $i = 45°$, and that many doubly peaked spectra were best represented by a model created at $i = 20°$, which further indicates that the profile type is not solely a function of i. It is simply not possible to assign inclination angles from profile types alone. This is the major finding of this investigation.

In the future, we plan to include more sophisticated density distributions in our computational code, eventually developing and testing realistic dynamical models. This will allow us to model the Be stars with variable, asymmetric emission profiles. We also plan a detailed study on the group of Be stars commonly called shell stars. This group of stars is characterized by emission lines in the Balmer series including a central absorption core that drops below the continuum (Hanuschik 1996). The central absorption core is thought to arise when a normal Be star is viewed nearly edge-on as disk material becomes optically thick along the line of sight. However, since some Be stars have been observed to transition between emission only phases and shell phases, shell spectra cannot be due to viewing angle alone (Porter & Rivinius 2003). Hanuschik (1996) suggests that a change in disk geometry, specifically the disk radius, may be the source of these transitions from shell to pure emission. Carciofi & Bjorkman (2008) recently studied the effect of disk temperature on the density distribution and concluded that a consideration of non-isothermal density structures was essential to properly predict observables. A thorough study of shell stars, including the variation of the width and central absorption width, is clearly needed. Our models, that include a self-consistent thermal structure along with more sophisticated density distributions with overdense and underdense volumes of disk gas, will allow this important group of Be stars to be investigated in detail in the future.

We are grateful to an anonymous referee whose comments and suggestions helped to improve the paper. We thank the Lowell Observatory for the telescope time used to obtain the Hα line spectra presented in this work. This research was supported in part by NSERC, the Natural Sciences and Engineering Research Council of Canada. C.T. acknowledges, with thanks, grant support from the Central Michigan University.

Facilities: Hall.

APPENDIX

CATALOG OF OBSERVED Hα PROFILES

Figure 8 shows spectra of the 69 Be star targets listed in Table 3. The spectra were obtained between 2005 and 2008, where the date of each observation is listed on each plot. The spectroscopic observations were acquired using a fiber-fed echelle spectrograph connected to the 42 inch John S. Hall Telescope at the Lowell Observatory located in Flagstaff, Arizona. The spectroscopic data were processed using standard routines developed specifically for the instrument used to acquire the observations (Hall et al. 1994). The reduced spectra in the Hα region have a resolving power of 10,000. The individual fluxes of all the spectra are also listed in Table 4.

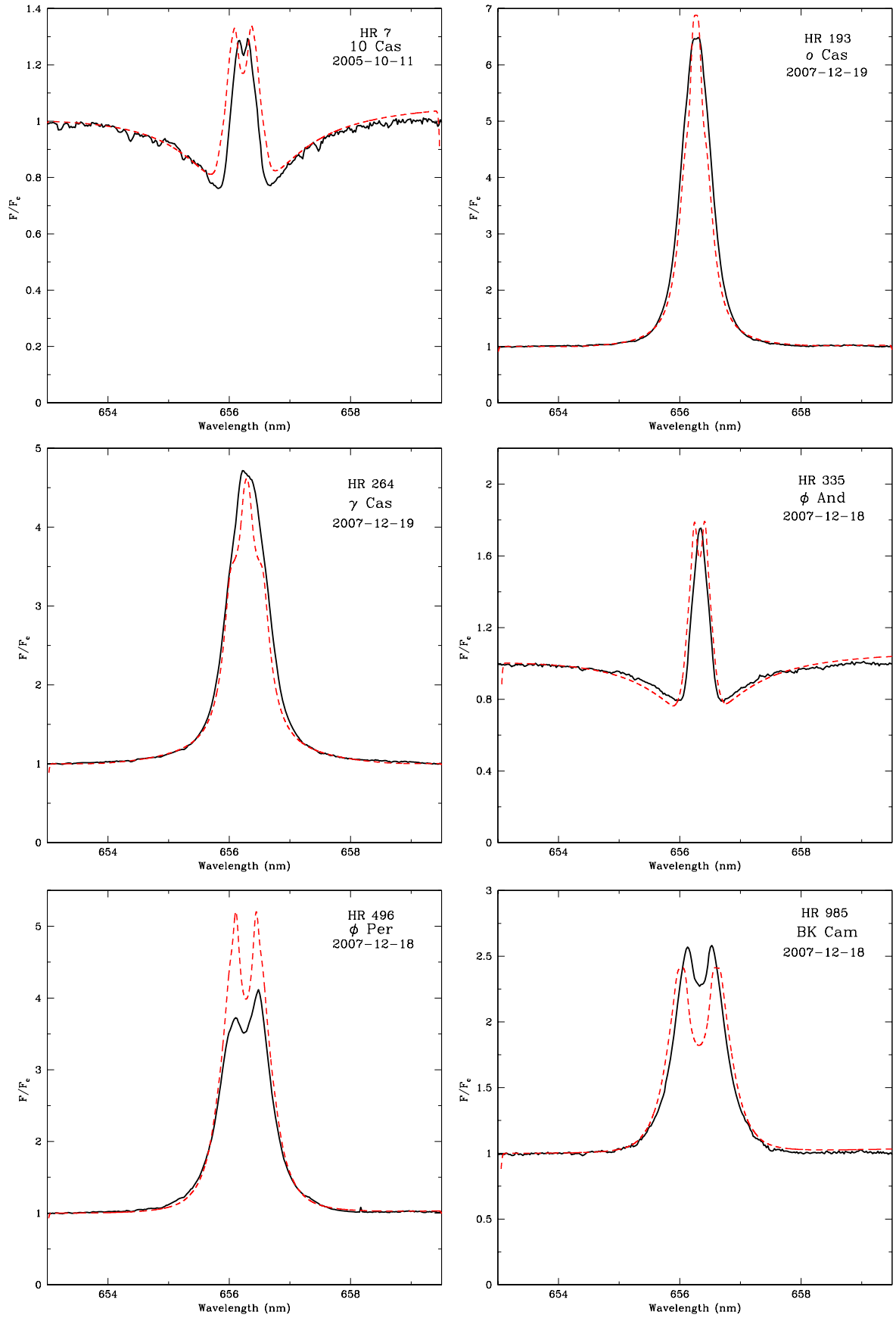

Figure 8. Observed Hα line emission spectra (solid lines) along with the theoretical line profiles (dotted lines) for different Be stars.
(A color version of this figure is available in the online journal.)

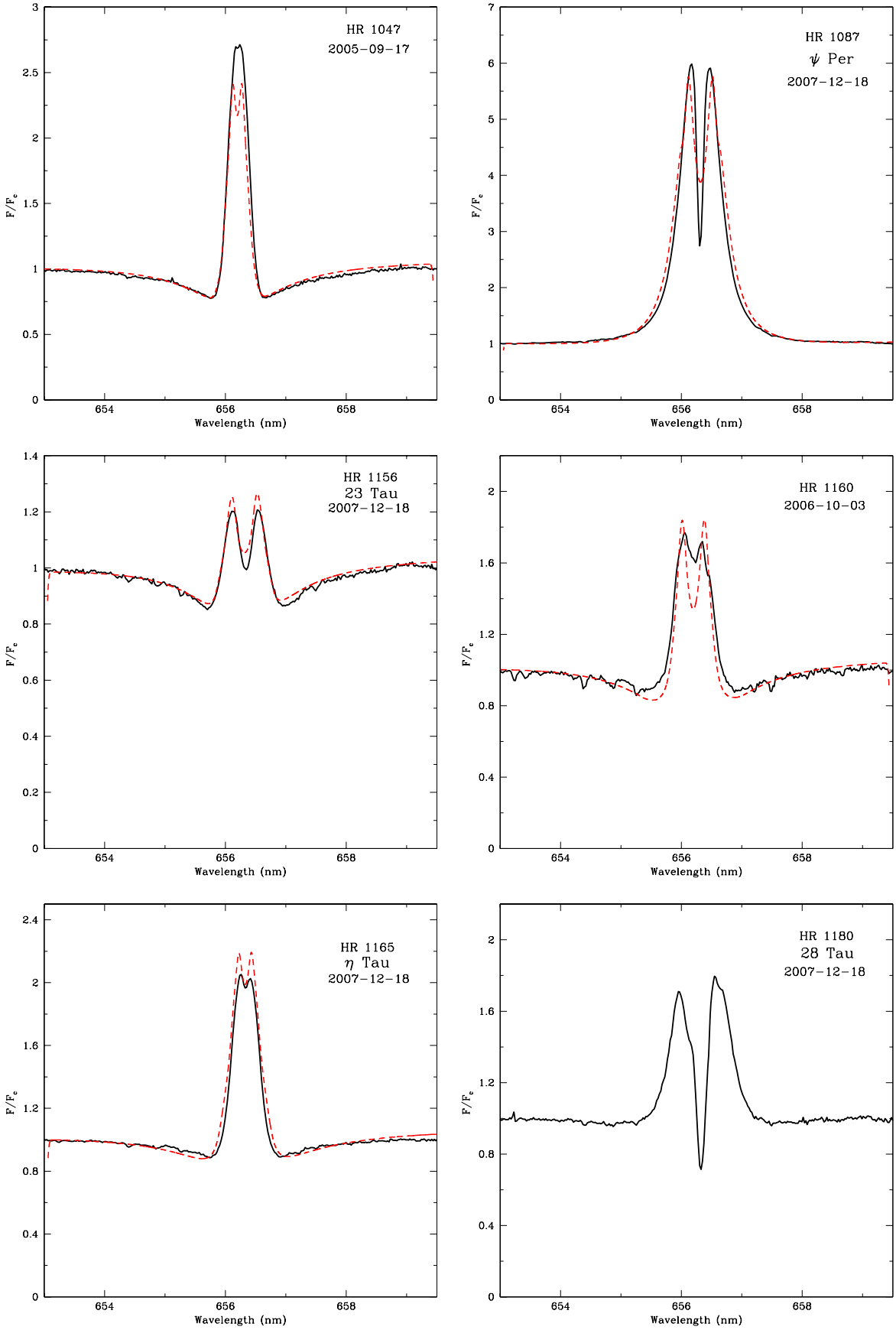

Figure 8. (Continued)

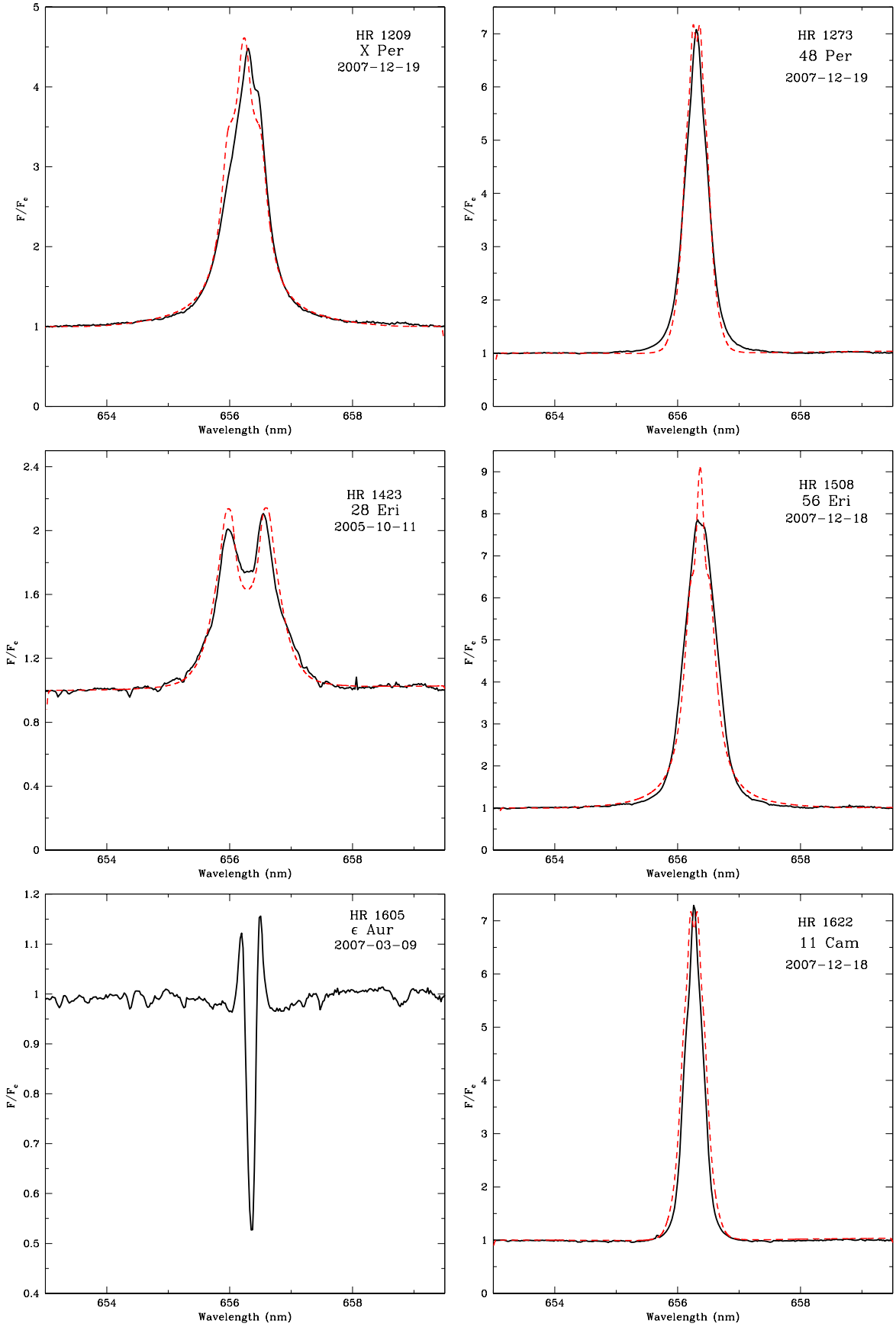

Figure 8. (Continued)

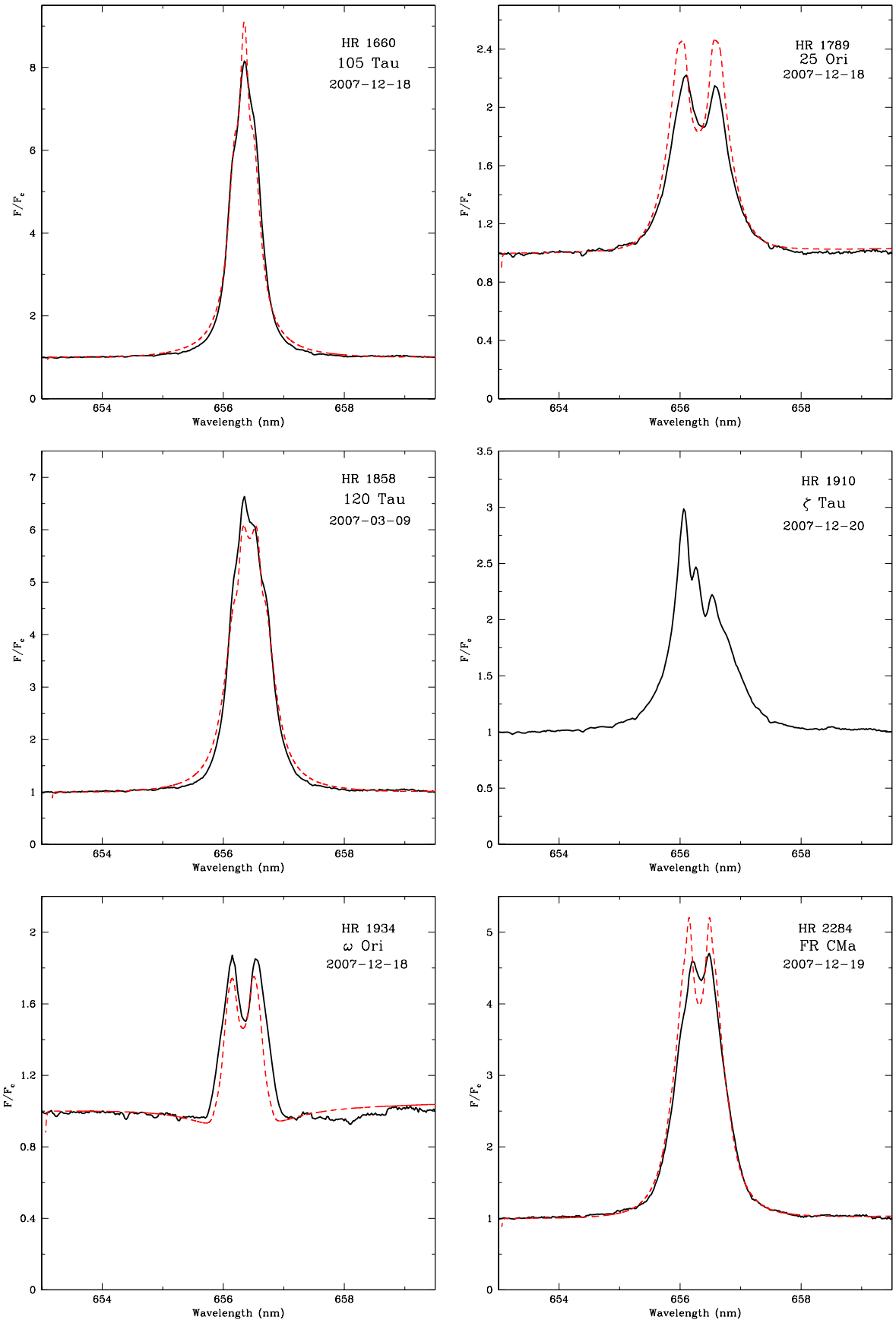

Figure 8. (Continued)

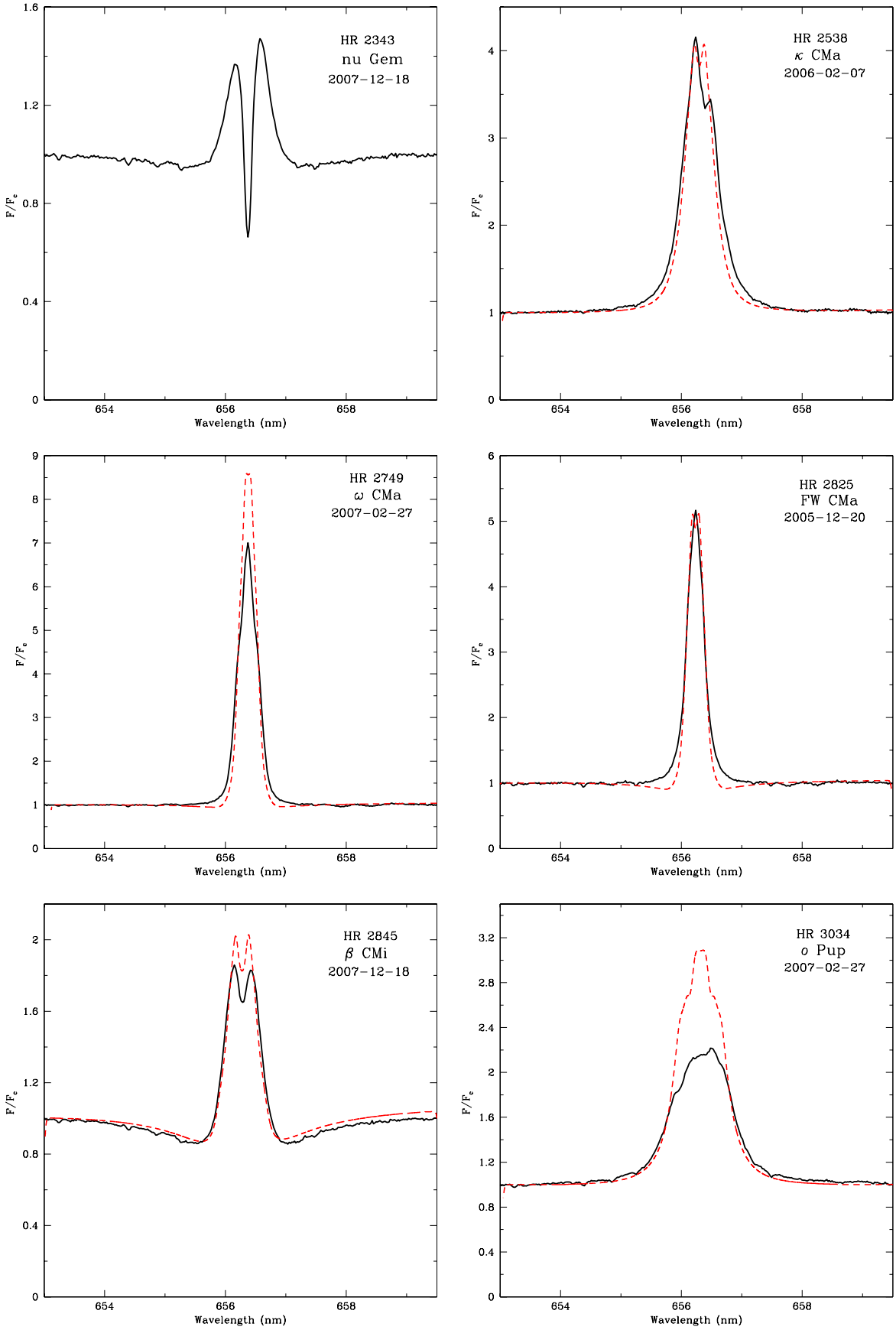

Figure 8. (Continued)

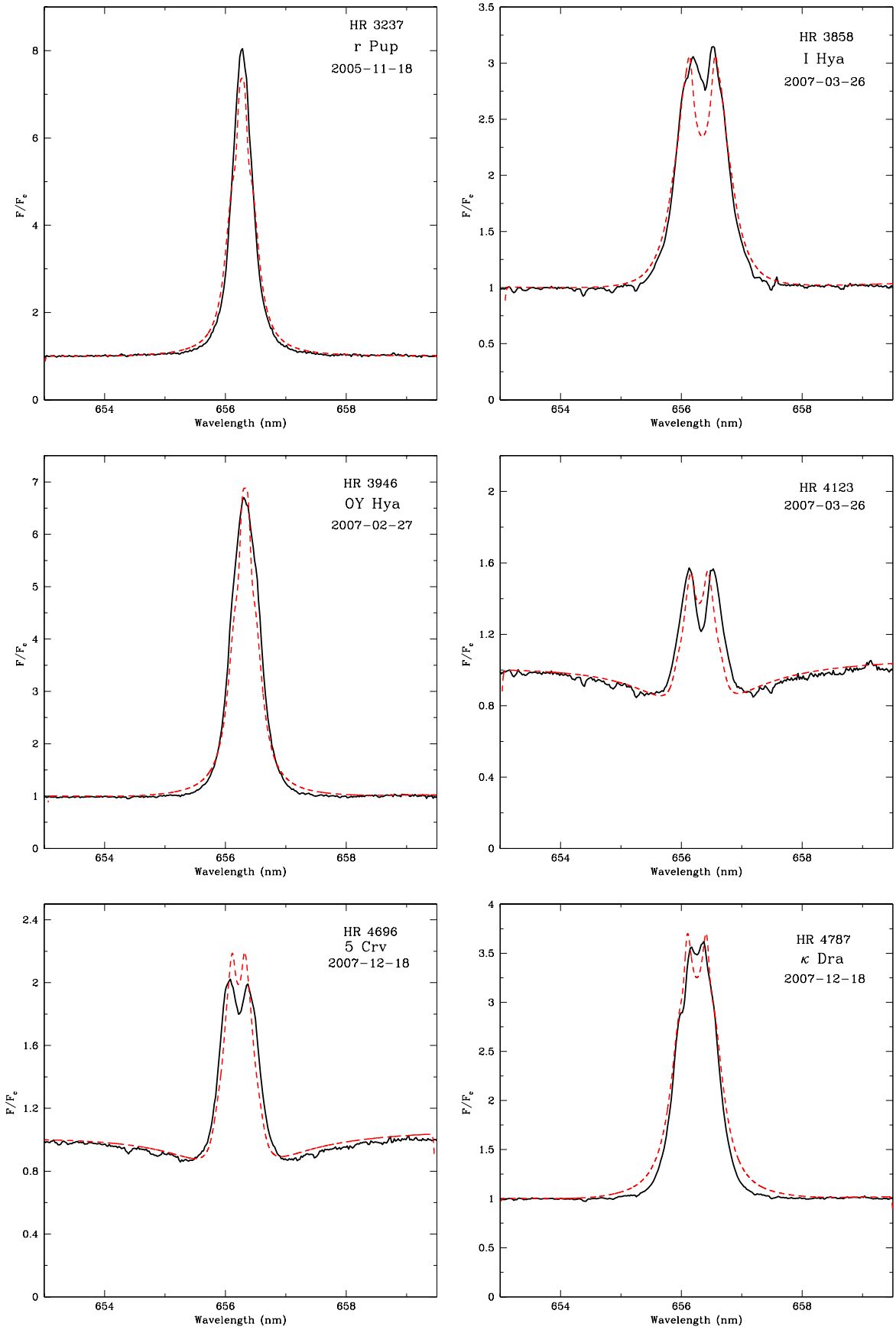

Figure 8. (Continued)

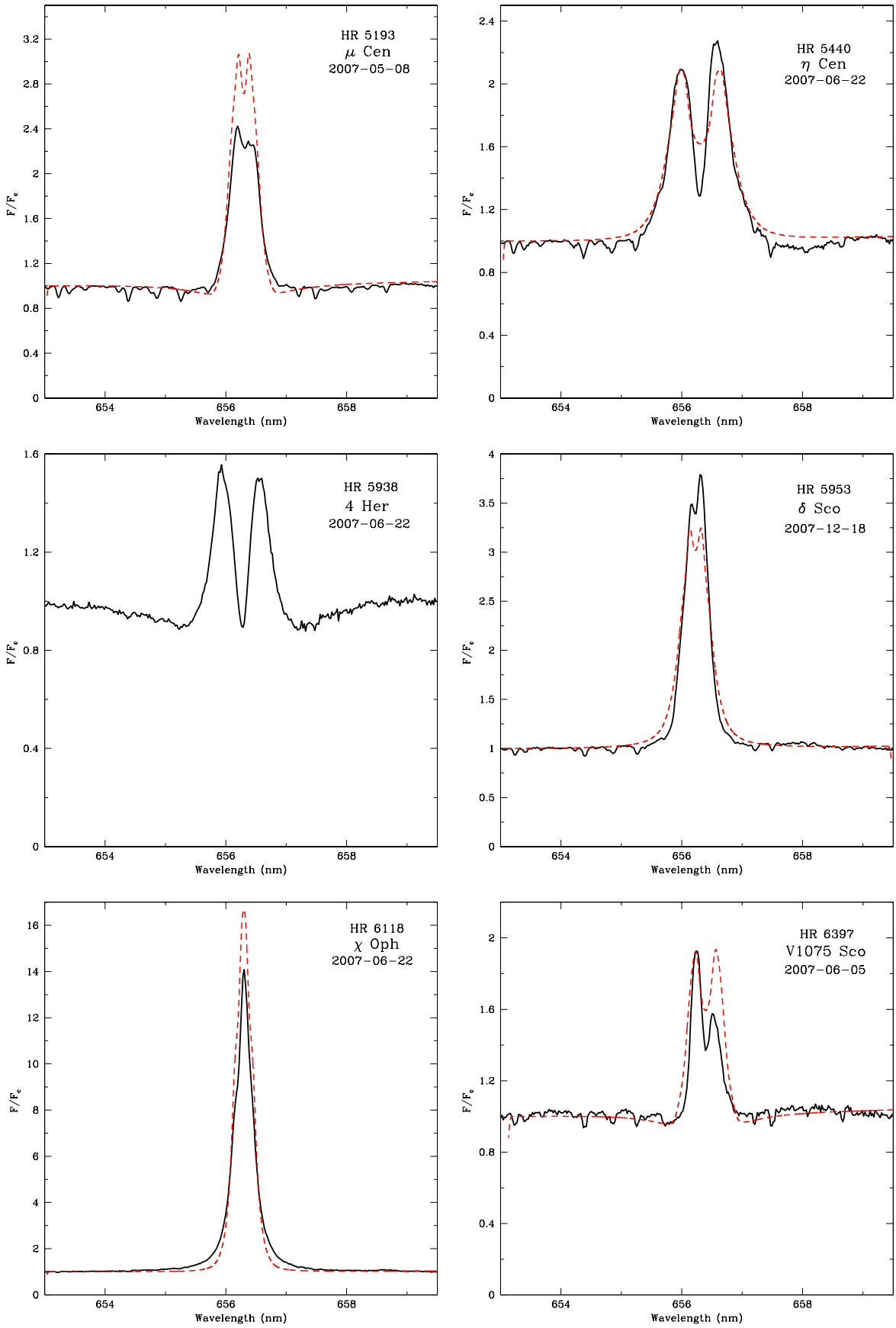

Figure 8. (Continued)

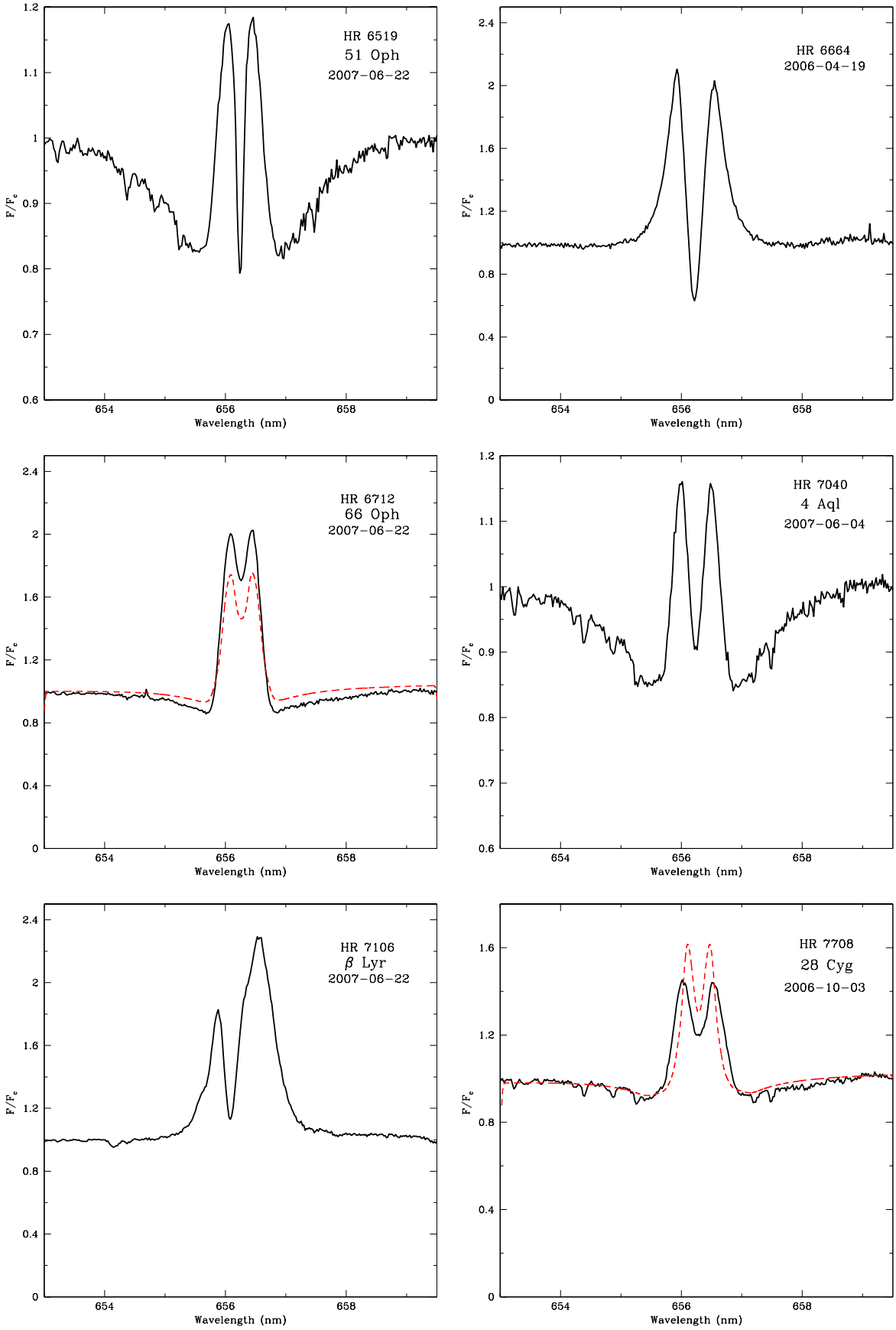

Figure 8. (Continued)

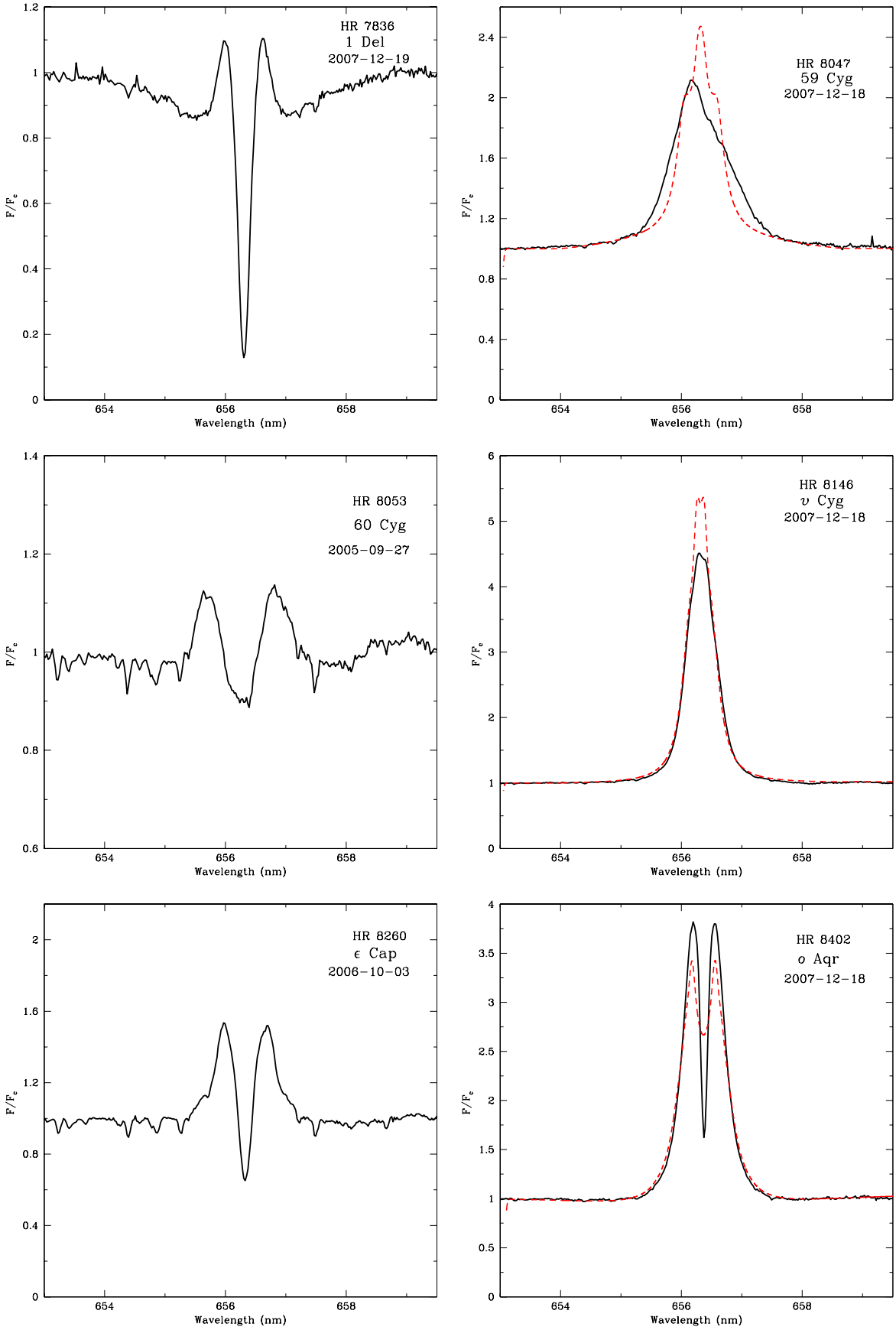

Figure 8. (Continued)

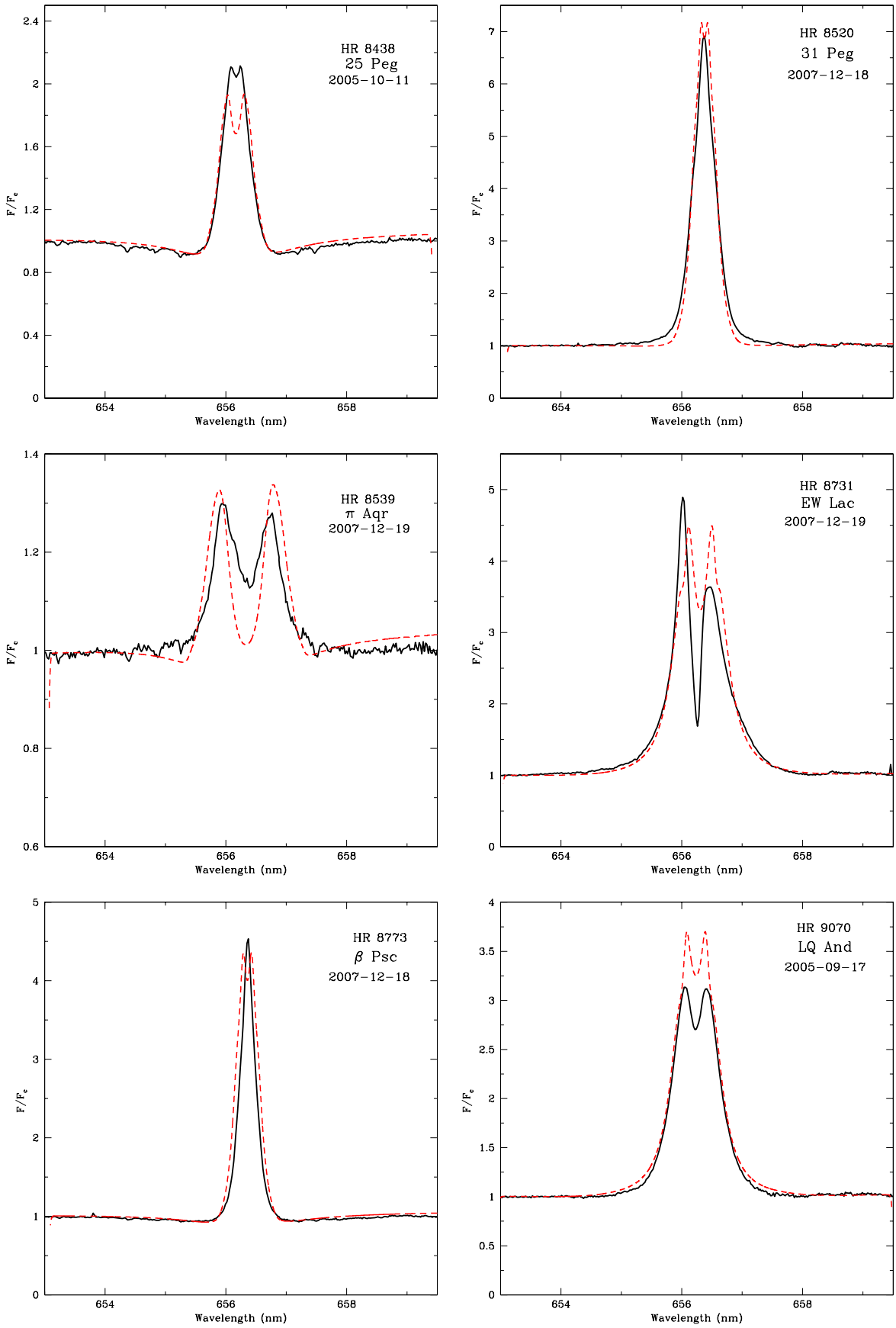

Figure 8. (Continued)

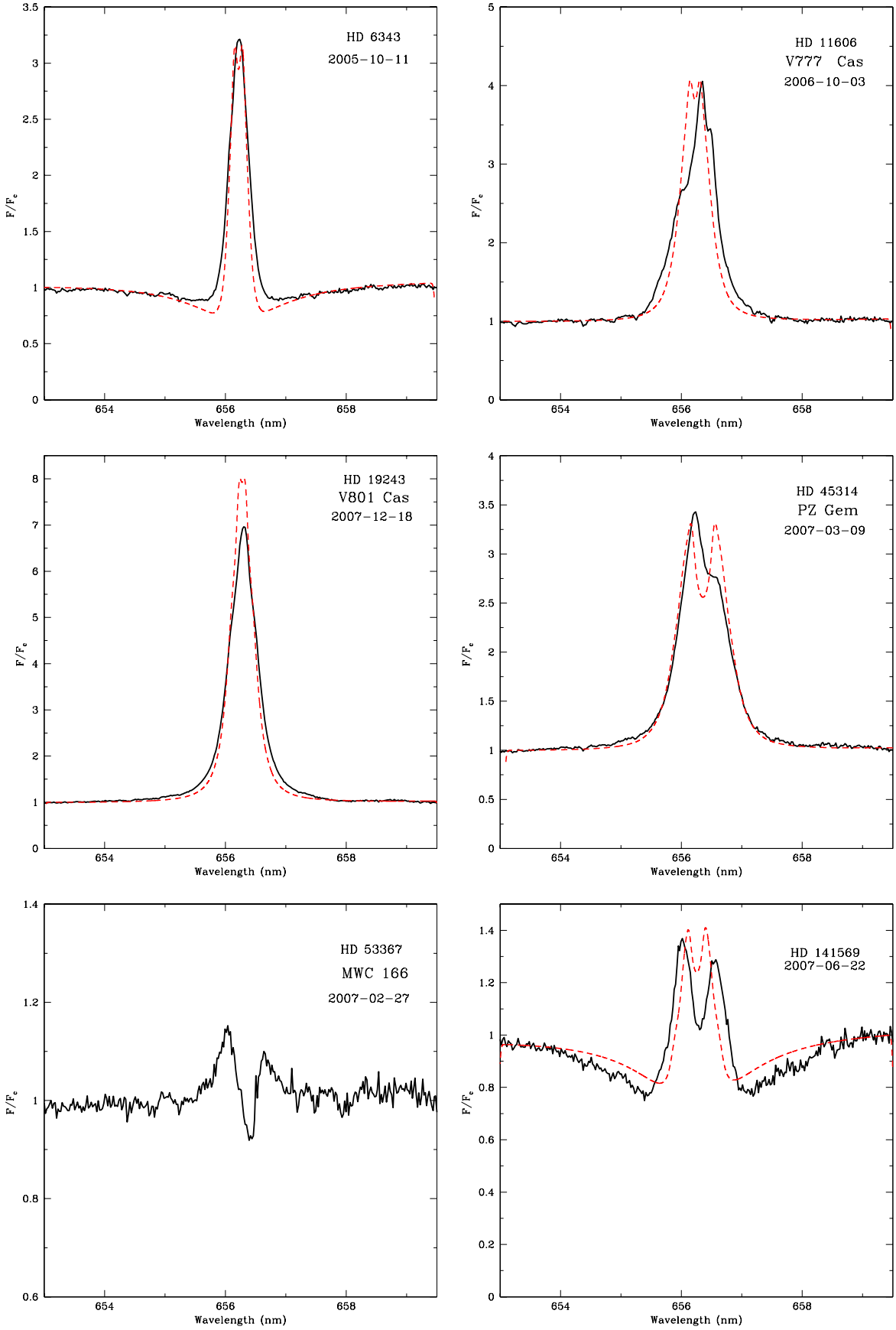

Figure 8. (Continued)

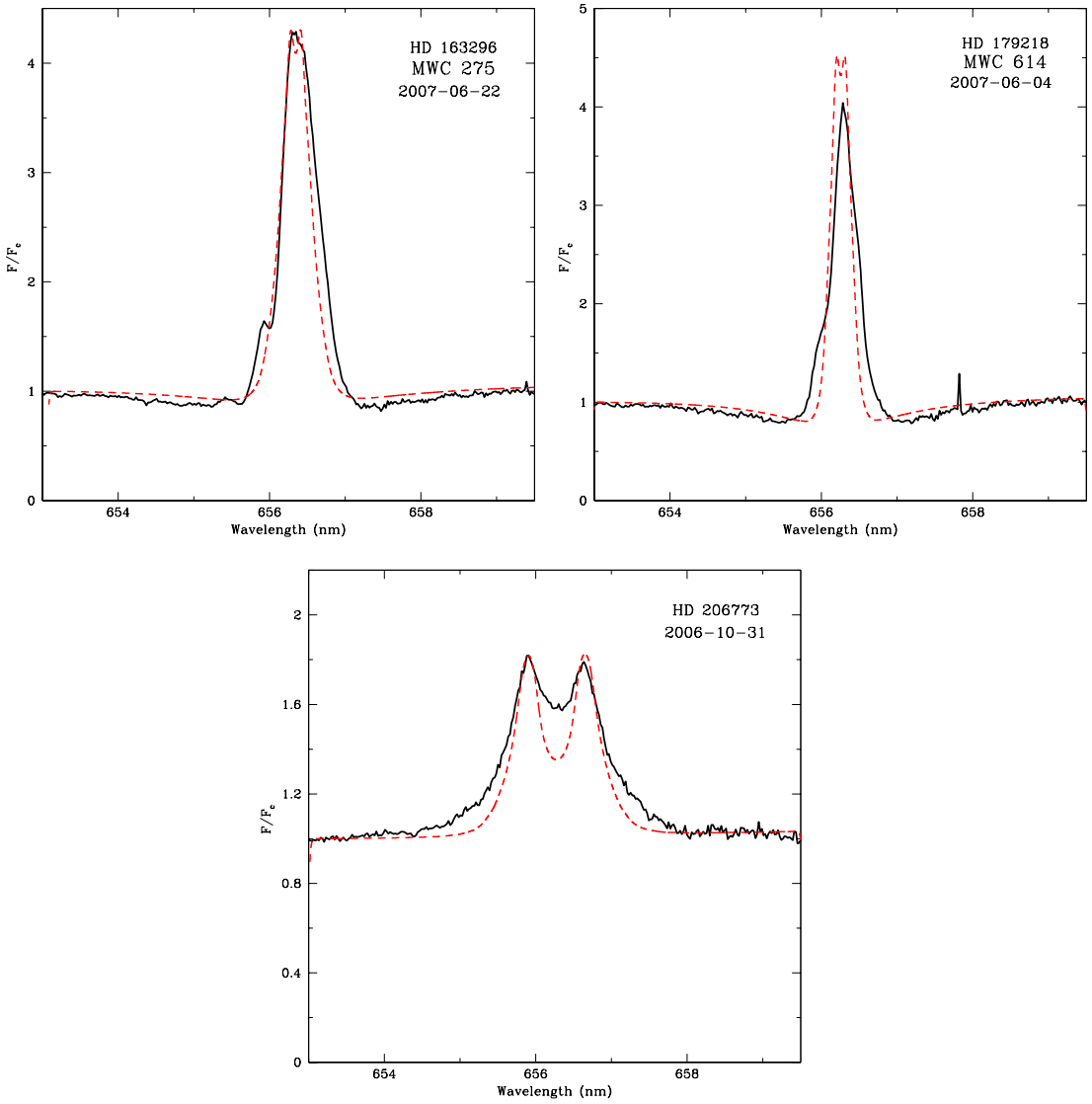

Figure 8. (Continued)

REFERENCES

Anders, E., & Grevesse, N. 1989, Geochim. Cosmochim. Acta, 53, 197
Anders, E., & Noels, A. 1993, Phys. Scr., T47, 133
Barker, P. K. 1982, ApJS, 49, 89
Barklem, P. S., & Piskunov, N. 2003, in IAU Symp. 210, Modelling of Stellar Atmospheres, ed. N. Piskunov, W. W. Weiss, & D. F. Gray (San Francisco, CA: ASP), E28
Carciofi, A. C., & Bjorkman, J. E. 2008, ApJ, 684, 1374
Carciofi, A. C., et al. 2009, A&A, 504, 915
Coté, J., & Waters, L. B. F. M. 1987, A&A, 176, 93
Cowley, A. P., & Marlborough, J. M. 1968, PASP, 80, 42
Cox, A. N. (ed.) 2000, Allen's Astrophysical Quantities (4th ed.; New York: Springer)
Cramer, N., et al. 1995, A&A, 301, 811
Cranmer, S. R. 2005, ApJ, 634, 585
Gulliver, A. F. 1997, ApJS, 35, 441
Hall, J. C., Fulton, E. E., Huenemoerder, D. P., Welty, A. D., & Neff, J. E. 1994, PASP, 106, 315
Hanuschik, R. W. 1986, A&A, 166, 185
Hanuschik, R. W. 1996, A&A, 308, 170
Hanuschik, R. W., Hummel, W., Sutorius, E., Dietle, O., & Thimm, G. 1996, A&AS, 116, 309
Harmanec, P. 2002, in ASP Conf. Ser. 279, Exotic Stars as Challenges to Evolution, ed. C. A. Tout & W. Van Hamme (San Francisco, CA: ASP), 221
Horne, K., & Marsh, T. R. 1986, MNRAS, 218, 761
Hummel, W., & Vrancken, M. 2000, A&A, 359, 1075
Iwamatsu, H., & Hirata, R. 2008, PASJ, 60, 749
Jones, C. E., Sigut, T. A. A., & Marlborough, J. M. 2004, MNRAS, 352, 841
Jones, C. E., et al. 2008, ApJ, 687, 598
Miroshnichenko, A. S., et al. 2001, A&A, 377, 485
Okazaki, A. T. 1997, A&A, 318, 548
Olson, G. L., & Kunasz, P. B. 1987, J. Quant. Spectrosc. Radiat. Transfer, 38, 325
Paploizou, J. C., Savonije, G. J., & Henrichs, H. F. 1992, A&A, 265, L45
Porter, J. M. 1996, MNRAS, 280, L31
Porter, J. M. 1999, A&A, 348, 512
Porter, J. M., & Rivinius, T. 2003, PASP, 115, 1153
Quirrenbach, A., et al. 1997, ApJ, 479, 477
Secchi, A. 1867, Astron. Nachr., 68, 63
Sigut, T. A. A., & Jones, C. E. 2007, ApJ, 668, 481
Slettebak, A. 1979, Space Sci. Rev., 23, 541
Struve, O. 1931, ApJ, 73, 94
Townsend, R. H. D., Owocki, S.P., & Howarth, I.D. 2004, MNRAS, 350, 189
Tycner, C., et al. 2005, ApJ, 624, 359
Tycner, C., et al. 2008, ApJ, 689, 461
Waters, L. B. F. M. 1986, A&A, 162, 121
Waters, L. B. F. M., Coté, J., & Lamers, H. J. G. L. M. 1987, A&A, 185, 206
Wisniewski, J. P., et al. 2007, ApJ, 656, L21